

Momentum transfer across shear flows in smoothed particle hydrodynamic simulations of galaxy formation

Takashi Okamoto,^{1★} Adrian Jenkins,^{1★} Vincent R. Eke,^{1★} Vincent Quilis^{2★} and Carlos S. Frenk^{1★}

¹*Institute for Computational Cosmology, Physics Department, Durham University, South Road, Durham DH1 3LE*

²*Departament d'Astronomia i Astrofísica, Universitat de València, 46100-Burjassot, Valencia, Spain*

Accepted 2003 June 25. Received 2003 June 25; in original form 2003 May 5

ABSTRACT

We investigate the evolution of angular momentum in smoothed particle hydrodynamic (SPH) simulations of galaxy formation, paying particular attention to artificial numerical effects. We find that a cold gas disc forming in an ambient hot gas halo receives a strong hydrodynamic torque from the hot gas. By splitting the hydrodynamic force into artificial viscosity and pressure gradients, we find that the angular momentum transport is caused not by the artificial viscosity but by the pressure gradients. Using simple test simulations of shear flows, we conclude that the pressure gradient-based viscosity can be divided into two components: one due to the noisiness of SPH and the other due to ram pressure. The former is problematic even with very high resolution, because increasing the resolution does not reduce the noisiness. On the other hand, the ram pressure effect appears only when a cold gas disc or sheet does not contain enough particles. In such a case, holes form in the disc or sheet, and then ram pressure from intra-hole hot gas causes significant deceleration. In simulations of galactic disc formation, star formation usually decreases the number of cold gas particles, and hole formation leads to the fragmentation of the disc. This fragmentation not only induces further angular momentum transport, but also affects star formation in the disc. To circumvent these problems, we modify the SPH algorithm, decoupling the cold gas phases from the hot ones, i.e. inhibiting the hydrodynamic interaction between cold and hot particles. This, a crude modelling of a multiphase fluid in SPH cosmological simulations, leads to the formation of smooth extended cold gas discs and to better numerical convergence. The decoupling is applicable in so far as the self-gravitating gas disc with negligible external pressure is a good approximation for a cold gas disc.

Key words: hydrodynamics – methods: numerical – galaxies: evolution – galaxies: formation.

1 INTRODUCTION

Understanding the formation of galactic discs is one of the most important unsolved problems in astrophysics. In the currently favoured cold dark matter (CDM) cosmological framework, in which structure builds up hierarchically (Davis et al. 1985), discs are assumed to form in the potential wells of virialized dark matter haloes through radiative cooling (White & Rees 1978; Fall & Efstathiou 1980; Dalcanton, Spergel & Summers 1997; Mo, Mao & White 1998; van den Bosch 2001). In this scenario, baryons are required to retain most of the angular momentum imparted to them by tidal torques in order for the resulting centrifugally supported discs to have realistic sizes.

The conservation of gas angular momentum is an important assumption made in semi-analytic modelling of disc formation (Kauffmann, White & Guiderdoni 1993; Somerville & Primack 1999; Cole et al. 2000; Nagashima et al. 2001; Okamoto & Nagashima).

However, to date, numerical simulations of galaxy formation starting from appropriate CDM initial conditions, and allowing just radiative cooling of the gas and no star formation or feedback, find that the infalling gas loses too much angular momentum. This results in discs forming which are much too small (e.g. Navarro & White 1994; Navarro, Frenk & White 1995). This problem is commonly called ‘the angular momentum problem’. The angular momentum losses arise during the hierarchical clustering process. At early times in a CDM-dominated universe, small dense dark matter haloes form. Radiative cooling is very efficient in these objects and a large fraction of the gas cools into them. As these gas-rich haloes merge to form larger haloes their incoming orbital angular momentum is

★E-mail: Takashi.Okamoto@durham.ac.uk (TO); A.R.Jenkins@durham.ac.uk (AJ); V.R.Eke@durham.ac.uk (VRE); Vicent.Quilis@uv.es (VQ); C.S.Frenk@durham.ac.uk (CSF).

drained by dynamical friction and exported to the dark matter at the outskirts of the new haloes. Much of the original angular momentum of the gas is lost through these processes by the time it reaches the middle and forms a disc.

Weil, Eke & Efstathiou (1998) and Eke, Efstathiou & Wright (2000) have shown that if cooling is suppressed until the host haloes are well established, then the numerical simulations yield much larger discs. Two ideas have been suggested which might prevent the early collapse of small protogalactic gas clouds. One is that cooling may be suppressed by feedback due to energy injected by stellar winds and supernovae. Simulations invoking very energetic feedback have illustrated the possibility of resolving the angular momentum problem in this way (Thacker & Couchman 2001; Sommer-Larsen, Götz & Portinari 2002). The second idea that has been suggested to prevent the formation of small protogalactic clouds is to invoke an alternative form of dark matter, ‘warm dark matter’, in which case the initial density field does not have small-scale fluctuations (Pagels & Primack 1982). Sommer-Larsen & Dolgov (2001) and Governato et al. (2002) have shown that galaxies formed in this model have larger discs and smaller bulges than in simulations with CDM. The angular momentum problem is potentially a strong clue which can help unravel the processes of galaxy formation and the complicated star formation and feedback processes involved. For this to be possible, however, we must be careful to understand the role of any numerical effects which may be important in determining the outcome of galaxy formation simulations.

Smoothed particle hydrodynamics (SPH) has been widely used to study galaxy formation (e.g. Katz, Hernquist & Weinberg 1992; Evrard, Summers & Davis 1994; Navarro, Frenk & White 1995; Steinmetz & Navarro 1999; Thacker & Couchman 2000; Steinmetz & Navarro 2002) both because its fully Lagrangian nature is suited to problems that need a wide dynamic range like galaxy formation, and because of its simplicity and robustness which make it easy to incorporate into N -body codes. Despite these attractive features, there are problems. First of all, most of the SPH implementations utilize an artificial viscosity to capture shocks (but see also Inutsuka 2002). This artificial viscosity can introduce numerical momentum and angular momentum transport, and spurious energy dissipation. Indeed, Sommer-Larsen & Dolgov (2001) found that the angular momentum of a simulated galaxy increased when they used higher resolution. Another problem arises from the intrinsic smoothing properties of SPH. Because SPH represents a fluid element by smoothing over neighbouring particles, it is not well-suited for treating large density and velocity gradients. This can be a serious problem when a cold gas disc forms through radiative cooling in an ambient hot gas at the virial temperature. In this situation, the cold gas disc is much denser than the hot gas and generally rotates faster than the ambient hot medium. In addition, because star formation can lead to a decrease in the number of particles in the disc (~ 90 per cent of baryonic matter becomes stars in a disc), the effective spatial resolution degrades with time, an effect which may play an important role at low redshift.

In this paper we investigate angular momentum transfer from a cold gas disc to the hot halo gas and its effect on the simulation outcomes. Although alternative techniques based on Eulerian approaches coupled with a grid refinement scheme – adaptive mesh refinement (AMR) – have been recently implemented in cosmology (Abel, Bryan & Norman 2000; Teyssier 2002, and references therein), we concentrate here on numerical effects in SPH simulations of galaxy formation because SPH is by far the most widely used method in this area.

The outline of this paper is as follows. A brief description of our simulation code is given in Section 2. In Section 3, we carry

out cosmological simulations of disc formation in a virialized halo, and then demonstrate there is angular momentum transfer from the cold gas disc to the ambient hot gas. A forensic study is performed in Section 4 using simplified simulations to find the source of the problem and the dependence on the numerical resolution. In Section 5 we propose that decoupling of cold gas from ambient hot gas can avoid the problems found in earlier sections. The effect of the decoupling is shown using simplified simulations and cosmological simulations. The results are summarized and discussed in Section 6.

2 THE CODE

We use a modified and extended version of the parallel `TREESPH` code `GADGET` (Springel, Yoshida & White 2001). Unless otherwise specified, we will use the novel formulation of SPH that manifestly conserves energy and entropy when appropriate (Springel & Hernquist 2002) throughout this paper. As shown in Springel & Hernquist (2002), this formulation greatly reduces numerical inaccuracies compared to the more commonly used formulations.

`GADGET` employs an artificial viscosity which is the shear-reduced version (Balsara 1995; Steinmetz 1996) of the ‘standard’ Monaghan & Gingold (1983) artificial viscosity. Lombardi et al. (1999) and Thacker et al. (2000) endorsed this form of the artificial viscosity. We set the parameter α that appears in equation (27) of Springel et al. (2001) to 0.75. We have checked that the choice of the value of this parameter hardly affects our results.

We also modify the gradient of the smoothing kernel from the public version of `GADGET` according to Thomas & Couchman (1992) to overcome the clumping instability (Schüssler & Schmitt 1981). `GADGET` adopts the kernel, W , so-called B_2 -spline (Monaghan 1985)

$$W(r, h) = \frac{8}{\pi h^3} \begin{cases} 1 - 6u^2 + 6u^3 & \text{for } 0 \leq u \leq 1/2, \\ 2(1 - u)^3 & \text{for } 1/2 < u \leq 1, \\ 0 & \text{for } u > 1, \end{cases} \quad (1)$$

where r and h are the particle separation and smoothing length, respectively, and $u = r/h$. Note that the smoothing kernel is defined over the interval $[0, h]$ and not $[0, 2h]$, as is more common. The kernel gradient vanishes at $u = 0$, i.e. the pressure gradient forces between two close SPH particles vanishes in the limit of small separation. We modify the gradient for $\leq 1/3$ so that even close pairs of SPH particles continue to repel each other, but leave the kernel itself unchanged,

$$\frac{dW}{du} = \frac{dW}{du} \left(u = \frac{1}{3} \right) = -\frac{16}{\pi h^3}, u \leq \frac{1}{3}. \quad (2)$$

Except in cosmological simulations, where we solve for the ionization, we assume a fixed mean molecular weight, $\mu = 0.59$, corresponding to a fully ionized gas of primordial composition. We use the adiabatic index $\gamma = 5/3$ throughout this paper.

3 COSMOLOGICAL SIMULATIONS OF DISC FORMATION

In order to study disc formation and to concentrate on the investigation of numerical angular momentum transfer, we wish to avoid the physical angular momentum losses which occur during hierarchical clustering as much as possible while retaining a degree of realism. To meet these requirements, we choose a halo, from a pre-existing N -body simulation, that is known to have a quiet merger history – the redshift of the last major merger is larger than 1. In addition, the gas is not allowed to cool radiatively until after $z = 1$. After this,

both cooling and star formation are allowed. This procedure completely suppresses the early formation of protogalactic clouds and leads to quiescent gas accretion for $z < 1$, with the result that a disc forms with a reasonable size (Weil et al. 1998; Eke et al. 2000). The details of the simulation are described in the following subsections.

3.1 Initial conditions

The background cosmology that we assume is a low-density, flat CDM universe (Λ CDM). This model is currently the favourite amongst hierarchical clustering models. We use the following choice of the cosmological parameters: $\Omega_0 = 0.3$, $h \equiv H_0/100 \text{ km s}^{-1} \text{ Mpc}^{-1} = 0.7$, $\lambda_0 \equiv \Lambda_0/(3H_0^2) = 0.7$ and $\sigma_8 = 0.9$. The baryon density, Ω_b , is set to 0.04 (Netterfield et al. 2002).

To generate our initial conditions, we use the resimulation technique introduced by Frenk et al. (1996). We first perform a dark matter only simulation in a $35.325 h^{-1} \text{ Mpc}$ periodic cube. On this scale, the density fluctuations are still in the linear regime at $z = 0$. Having completed this simulation, we then select a dark halo that has a quiet merger history. The mass of the halo is about $1.3 \times 10^{12} h^{-1} M_\odot$ within the sphere which has virial overdensity, $\delta_{\text{vir}} = 337$ at $z = 0$. To make the new initial conditions, the initial density field of the parent simulation is recreated and appropriate additional short wavelength perturbations are added to the region out of which the halo forms. In this region we also place SPH particles in a ratio of 1:1 with dark matter particles. The region external to this was populated with high-mass dark matter particles, the function of which is to reproduce the appropriate tidal fields. The initial redshift of the simulation is 50. The masses of the SPH and high-resolution dark matter particles are $\sim 2.6 \times 10^6 h^{-1} M_\odot$ and $\sim 1.7 \times 10^7 h^{-1} M_\odot$, respectively.

The gravitational softening length for the SPH particles is kept fixed in comoving coordinates for $z > 3$; after this it is frozen in physical units to a value of 0.5 kpc, in terms of the ‘equivalent’ Plummer softening given in Springel et al. (2001). The gravitational force obeys the exact r^{-2} law at $r > 2.8\epsilon$. The softening lengths for all particles are defined as $\epsilon_p = \epsilon_{\text{sph}}(m_p/m_{\text{sph}})^{1/3}$, where m_p is the particle mass of a particle ‘p’ and ϵ_{sph} and m_{sph} are the softening and mass of the SPH particles, respectively. We do not allow the smoothing length to become smaller than a minimum value of $h_{\text{min}} = 1.4\epsilon$.

3.2 Cooling and star formation

For $z < 1$ the cooling/heating rate and ionization state of each particle are calculated assuming collisional ionization equilibrium and the presence of an evolving but uniform UV background (Haardt & Madau 1996) by using the fitting formula provided by Theuns et al. (1998). A primordial composition for the gas is assumed. Inverse Compton cooling is also considered at $z < 1$ although the effect is minor. Because we do not include molecular cooling, the coolest gas typically has a temperature $T_{\text{cold}} \simeq 10^4 \text{ K}$. We define the gas in an overdense region that has a temperature $T < 3 \times 10^4 \text{ K}$ as ‘cold gas.’

Cold gas particles are eligible to form stars when the following criteria are satisfied: (i) the gas particle is in a converging flow ($\nabla \cdot \mathbf{v}_i < 0$) and (ii) the density of the gas particle is above a threshold density ($\rho_i > \rho_{\text{th}}$). We use $\rho_{\text{th}} = 5 \times 10^{-25} \text{ g cm}^{-3}$. The value that we adopt is higher than the typical value used in other cosmological simulations, $2 \times 10^{-25} \text{ g cm}^{-3}$ (Katz, Weinberg & Hernquist 1996). This choice allows us to have sufficient cold gas to observe the numerical effect on the cold phase. Note that Buonomo et al. (2000) found that the criterion on the velocity divergence has

no sizeable effect on their results, and so criterion (i) may not be needed. We ignore the Jeans condition, used by some other authors (e.g. Katz et al. 1996), for reasons detailed below.

The Jeans condition is usually denoted as

$$h_i/c_s > t_{\text{dyn}}, \quad (3)$$

where h_i , c_s , and $t_{\text{dyn}} = (4\pi G\rho_i)^{-1/2}$ are the smoothing length, the sound speed, and the dynamical time of the gas particle ‘i,’ respectively. As the h_i values have no direct physical significance in the SPH formalism, and depend for example on the particle mass, adopting such a Jeans condition as given above would introduce an unphysical resolution-dependence into the simulations.

In fact, this Jeans condition should be regarded as determining the resolution limit rather than as a star formation criterion. Bate & Burkert (1997) have shown that if the minimum resolvable mass $\sim 2N_{\text{ngb}}m_{\text{sph}}$, where N_{ngb} is the number of neighbours used in the SPH calculation, becomes larger than the local Jeans mass, $\sim G^{3/2}\rho^{-1/2}c_s^3$, artificial fragmentation may occur, and real fragmentation will definitely be suppressed. In our adopted SPH implementation, the smoothing length, h_i , is defined as $(4\pi/3)h_i^3\rho_i = m_{\text{sph}}N_{\text{ngb}}$, and one finds combining these relations that the above resolution limit is equivalent to

$$\frac{h_i}{c_s} < \pi^{1/2} \left(\frac{3}{\pi} \right)^{1/3} t_{\text{dyn}} \simeq \pi^{1/2} t_{\text{dyn}}. \quad (4)$$

It is clear that the condition represented by equation (3) is hardly satisfied if the condition represented by equation (4) is satisfied. We adopt $N_{\text{ngb}} = 40$ in this paper, and this gives a gas temperature of $T = 10^4 \text{ K}$ that for densities below $\rho_{\text{max}} \sim 1.2 \times 10^{-25} \text{ g cm}^{-3}$ the SPH treatment of the gas is reliable. Note that this is well below our threshold density ρ_{th} for star formation. Therefore, our results may be affected by artificial effects because of insufficient mass resolution.

When a gas particle is eligible to form stars, the star formation rate (SFR) for a particle ‘i’ is

$$\frac{d\rho_*}{dt} = c_* \frac{\rho_i}{t_{\text{dyn}}}, \quad (5)$$

where c_* is a dimensionless SFR parameter. This formula corresponds to the Schmidt law that implies an SFR proportional to $\rho_i^{1.5}$. The value of c_* controls the star formation efficiency. The physics of star formation is not understood well enough to predict the value of this parameter. It is known for spiral galaxies that the star formation time-scale is long compared to the dynamical time-scale, so to mimic this the value of c_* must be significantly less than unity. We assume a value of $c_* = 0.05$ throughout this paper. This is consistent with the relatively small values of c_* used in simulations of disc formation (e.g. Katz 1992; Weil et al. 1998; Thacker & Couchman 2000). For an SPH particle of mass m_{gas} , which is eligible to form a star of mass m_* , the probability of this event occurring during a time-step Δt is given by

$$p_{\text{sf}} = \frac{m_{\text{gas}}}{m_*} \left[1 - \exp \left(-\frac{c_* \Delta t}{t_{\text{dyn}}} \right) \right]. \quad (6)$$

We use two star formation recipes to study the dependence of the results on the star formation scheme and also the number of particles left in a cold gas disc. In the first recipe, a gas particle is completely converted into a stellar particle during Δt so that $m_{\text{gas}}/m_* = 1$ in equation (6). We call a simulation using this star formation scheme a ‘conversion run’. The other recipe allows an initial SPH particle to spawn up to three stellar particles with mass of $m_{\text{sph}}/3$, where m_{sph}

is the original mass of the SPH particle, so that the values possible for m_{gas}/m_* are 3, 2 or 1. This scheme reduces the rapid decrease in the number of cold gas particles in the disc due to star formation, and helps counter the large drop in the SPH spatial resolution which otherwise occurs as the cold gas is used up. The simulation which employs this scheme is dubbed a ‘spawning run.’

3.3 Results

In Fig. 1, we show the distributions of stars and cold gas in the galaxy at $z = 0$. The galaxy in the spawning run has a smoother stellar distribution than in the conversion run, as is expected. Although the galaxy in the conversion run has a stronger bar, we cannot find any significant difference in the distribution of the stars when we compare the surface density profiles of these galaxies.

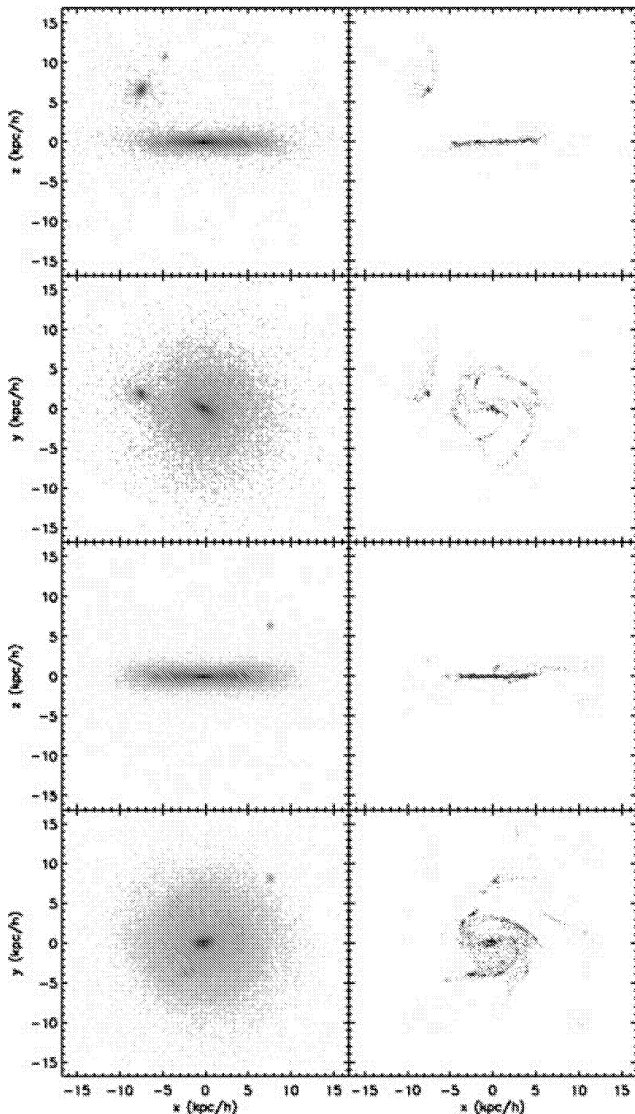


Figure 1. Distribution of stars and cold gas in the galaxy at $z = 0$. The upper four panels and the lower four panels are for the conversion run and the spawning run, respectively. The left-hand panels show the stellar distributions and the right-hand panels show the cold gas distributions. The grey-scale is coded by surface density and three dimensional density for stars and cold gas, respectively. The z -direction is chosen so that the z -axis becomes parallel to the stellar angular momentum of each galaxy.

However, the morphologies of the cold gas discs are quite different. The cold gas disc in the conversion run has a core and ring structure: the cold gas disc has large holes and most of the cold gas particles are found in dense filaments. The cold gas disc in the spawning run is perhaps more realistic with spiral arm-like features, though a large fraction of the cold gas lives in the arms. One might think that the fragmentation is caused by the Toomre instability. However, we find when we calculate the value of Toomre’s Q -parameter for the azimuthally averaged surface gas density that $Q > 1$ is satisfied everywhere and at all redshifts. Because of efficient star formation, the gas surface density never reaches high values. Having ruled out the Toomre instability we need to examine the time-evolution of the gas distributions to understand the physical or numerical mechanisms that cause the break up of the cold gas discs.

The distributions of the cold gas particles are shown in Fig. 2 for several redshifts in each simulation. We find that the core–ring structure is very common, regardless of the star formation scheme.

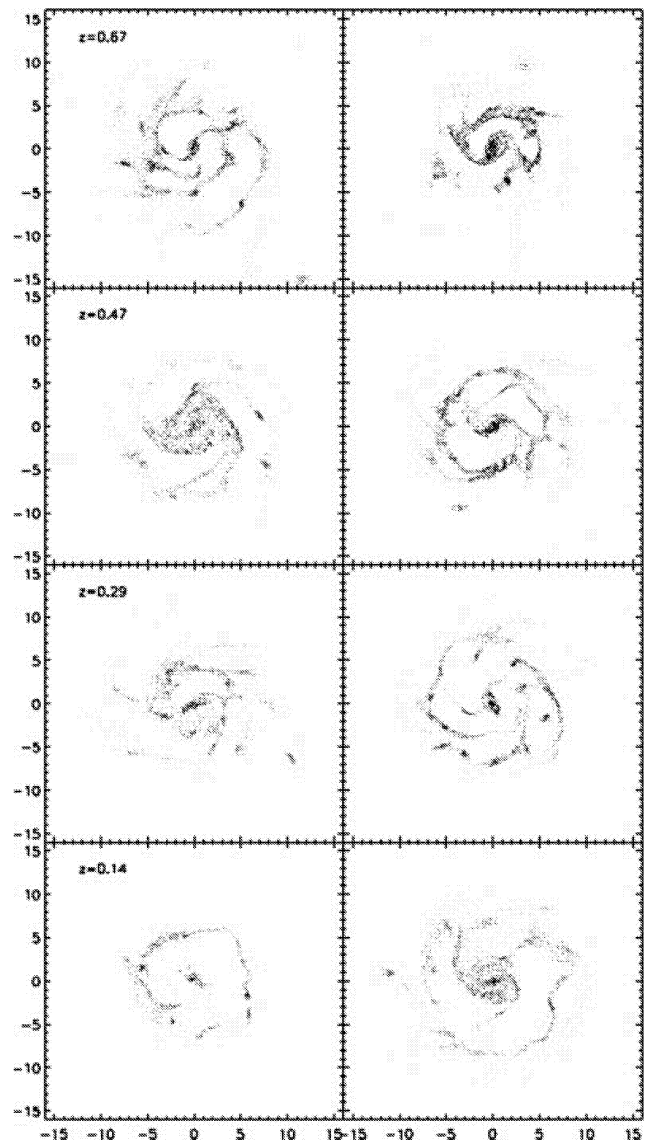


Figure 2. Face on views of the distribution of the cold gas. The left- and right-hand panels show the galaxy in the conversion run and spawning run, respectively.

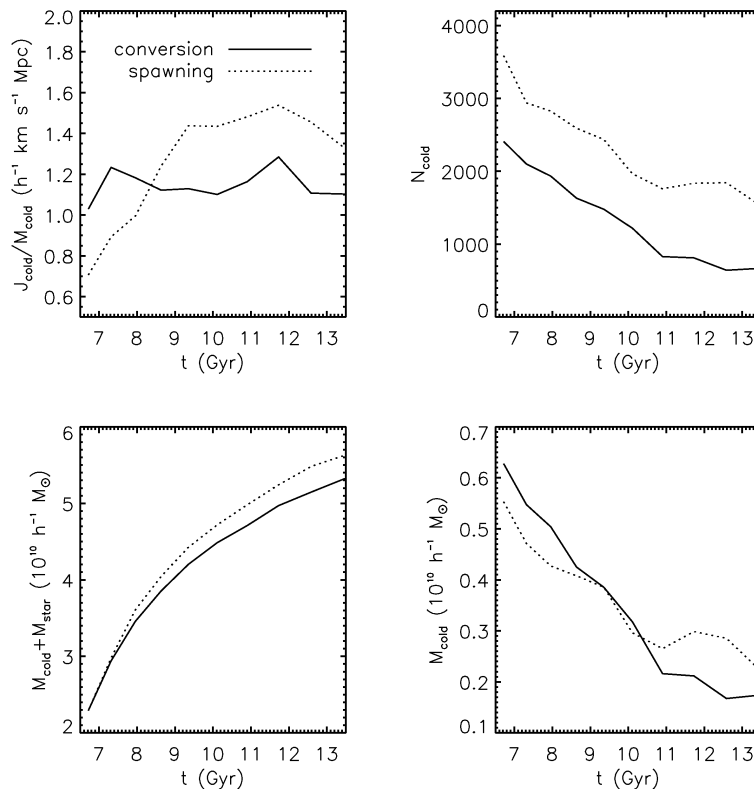


Figure 3. Evolution of the cold gas disc. The upper left-hand, upper right-hand, lower right-hand and lower left-hand panels show the specific angular momentum of the cold gas disc, the number of cold gas particles in the discs, the mass in the stars and cold gas (integrated cooling rate), and the mass of the cold gas disc, respectively, as a function of the age of the universe. The solid and dotted lines indicate the conversion and spawning run, respectively.

The spawning galaxy has a larger-sized cold gas disc at lower redshift than the conversion galaxy. This is consistent with the idea that there is angular momentum transfer away from cold gas in a way that depends on the number of the cold gas particles.

Because star formation turns low angular momentum gas particles into collisionless stellar particles, and the gas particles that accrete on to the disc later tend to have larger angular momenta, the specific angular momentum of the cold gas disc should monotonically increase with time. We plot the evolution of the specific angular momentum of the cold gas disc in Fig. 3. Here, we consider the material in a sphere of radius $20 h^{-1}$ kpc, which is centred on the galaxy centre at each redshift. The specific angular momentum for the conversion run shows surprisingly little evolution; it is nearly constant. In contrast, the angular momentum of the cold gas disc in the spawning run increases monotonically except for the last few Gyr. This indicates that more angular momentum is lost from the cold gas disc in the conversion run compared to in the spawning run.

The lower left-hand panel of Fig. 3 shows the integrated cooling rates (the mass in stars and cold gas at each redshift) in the galaxies. The figure shows that the cooling in the conversion run is suppressed relative to the spawning run. This indicates that a significant amount of angular momentum from the cold gas disc in the conversion run has been transferred to the ambient hot gas, and that the cooling rate has decreased because the hot gas has been puffed up by this ‘angular momentum feedback’. Because the difference in the amount of cold gas in the discs between the two simulations is small, the difference in the masses of the cooled baryon (i.e. cold gas and stars) is mainly due to the difference in the masses of stellar discs. By comparing the evolution of the angular momenta of the cold gas discs and the

number of cold gas particles in the discs (upper right-hand panel of Fig. 3), one might draw a naive conclusion that at least 2000 cold gas particles are needed to suppress the angular momentum transfer. However, we have to understand the mechanism that causes the angular momentum transfer and the fragmentation of the cold gas disc before we can reach definite conclusions.

To this end, we next investigate the hydrodynamic torques acting on the cold gas particles. In Fig. 4, we plot the azimuthally averaged specific hydrodynamic torques acting on the cold gas particles for the spawning simulation for five radial bins. The negative value indicates that the torque spins down the rotation of the disc. As expected from Fig. 3, the absolute magnitude of the torque is larger at lower redshift. Surprisingly, the torque is dominated not by the artificial viscosity but by the contribution to the force due to pressure gradients. The total hydrodynamic torques normalized by the angular momenta of the cold gas discs (τ_z/J_z) at $z = 0$ are -0.84 and -0.90 Gyr^{-1} for the conversion and spawning runs, respectively. This means that the hydrodynamic torque can stop the rotation completely in only ~ 1 Gyr. While the number of the cold gas particles in the spawning run is more than twice as large as that in the conversion run, both discs receive comparable torques at $z = 0$. This implies that the strength of the hydrodynamic torque is defined by the distribution (morphology) of the cold gas as well as the number of the cold gas particles in the disc.

To know whether there is significant angular momentum transfer between the cold gas particles at different radii, we calculate the instantaneous hydrodynamic torque acting on the cold gas disc and ignore the interaction between the cold ($T < 3 \times 10^4 \text{ K}$) and hot ($T > 10^5 \text{ K}$) phases. Fig. 5 shows the original torque that is identical

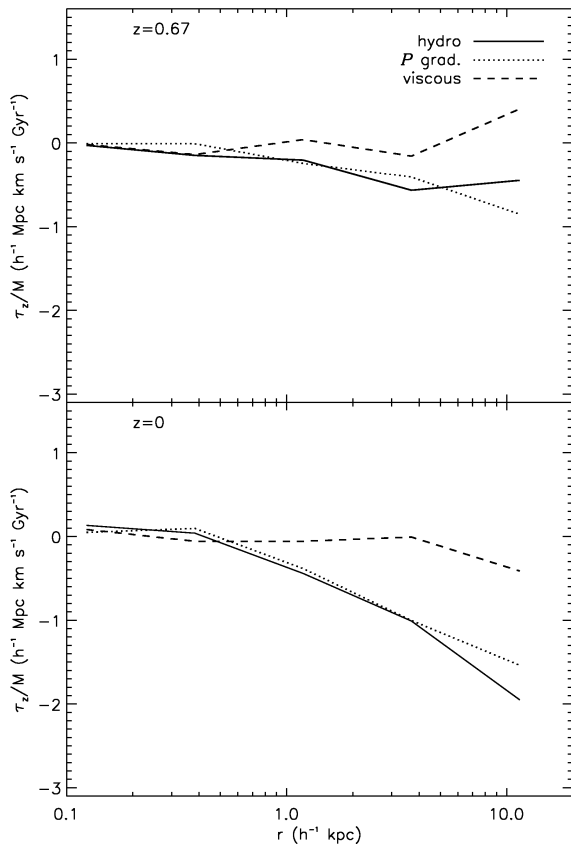


Figure 4. The hydrodynamic torques acting on the cold gas particles in the disc. The results for the spawning run are shown. Azimuthally averaged specific torques parallel to the angular momentum of the disc are plotted as functions of radius. The solid line represents the total hydrodynamic torque. This torque is decomposed into the torque from pressure gradient force (dotted) and that from the artificial viscosity (dashed).

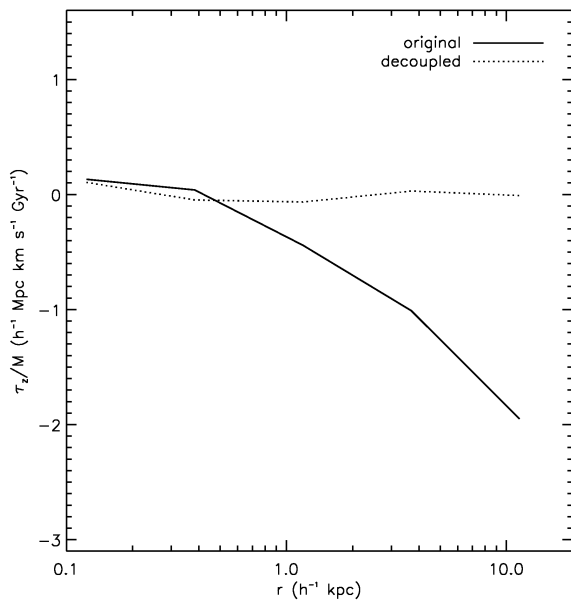


Figure 5. The hydrodynamic torque acting on the cold gas particles in the disc in the spawning run. The solid line is identical to the solid line in the lower panel of Fig. 4. The dotted line shows the torque when we ignore the interaction between the cold gas ($T < 3 \times 10^4$ K) and the hot gas ($T > 10^5$ K) particles.

to the solid line in the lower panel of Fig. 4 and the torque ignoring the hot gas. We find that the hydrodynamic torque becomes almost 0 at all radii when we decouple the cold and hot phases instantaneously. There is no significant transport of angular momentum within the cold gas itself. This confirms results from previous studies, which insist that the angular momentum transfer in the galactic disc itself cannot be a serious problem over a Hubble time when the shear-reduced artificial viscosity is adopted (e.g. Steinmetz 1996). Unfortunately, all test simulations have been performed in the absence of a surrounding (hot) medium.

As our results indicate that the artificial viscosity is not very important for the angular momentum transfer, the transfer may be caused by fragmentation or may cause the fragmentation. We will investigate this point using simplified simulations in the next section. We note that the gravitational torque acting on the cold gas disc is also significant when the cold gas is fragmented.

4 SIMPLIFIED SIMULATIONS

4.1 Shear flows

Several authors have presented shear flow tests using SPH, and their results are promising (Lombardi et al. 1999; Thacker et al. 2000). However, these studies have focused primarily on the variation resulting from using different SPH implementations. Here, we consider the impact of varying numerical resolution upon the momentum transferred across sharp velocity gradients, with or without associated sharp density gradients.

4.1.1 A single temperature test

We use simulations of a periodic cube of side 10 kpc, containing $10^{10} M_{\odot}$ of gas, to investigate the SPH transfer of momentum across a discontinuity in the velocity field. The gas is all given a temperature of 10^6 K. Particles in the central slab with $|z| < 0.3$ kpc are given a velocity of $v_x = 50$ km s $^{-1}$, and the remaining gas is set up with $v_x = -50$ km s $^{-1}$. At this relative velocity of 100 km s $^{-1}$, it takes ~ 100 Myr to cross the box. The self-gravity of the gas is ignored for simplicity, and replaced with an external potential of the form

$$\Psi(z) = -10000 \left[\cos\left(\frac{2\pi z}{L_{\text{box}}}\right) - 1 \right] (\text{km s}^{-1})^2, \quad (7)$$

where L_{box} is the side-length of the simulation box. The choice of external potential is not very important because the transfer of momentum is not greatly affected by the size of the instabilities that it suppresses. To generate relaxed initial conditions, we first distribute particles using the rejection method, assuming hydrostatic equilibrium, to calculate the density. This system is evolved without any shear, while damping the particle temperature and velocity until a relaxed state is reached. Then the shear is introduced and the tests are commenced. Simulations have been run with $(N_{\text{gas}}, N_{\text{ngb}}) = (32^3, 40), (64^3, 40)$ and $(64^3, 320)$. A single variant of SPH has been used for the runs in this subsection, but we do consider some other popular flavours with different symmetrizations in Section 4.1.3.

We have also used the three-dimensional Eulerian fixed-grid hydrodynamic code described by Quilis, Ibáñez & Sáez (1996) to provide a comparison. This finite difference (FD) code employs a Riemann solver to compute the numerical viscosity, thus removing the need for an artificial viscosity, and has already been used

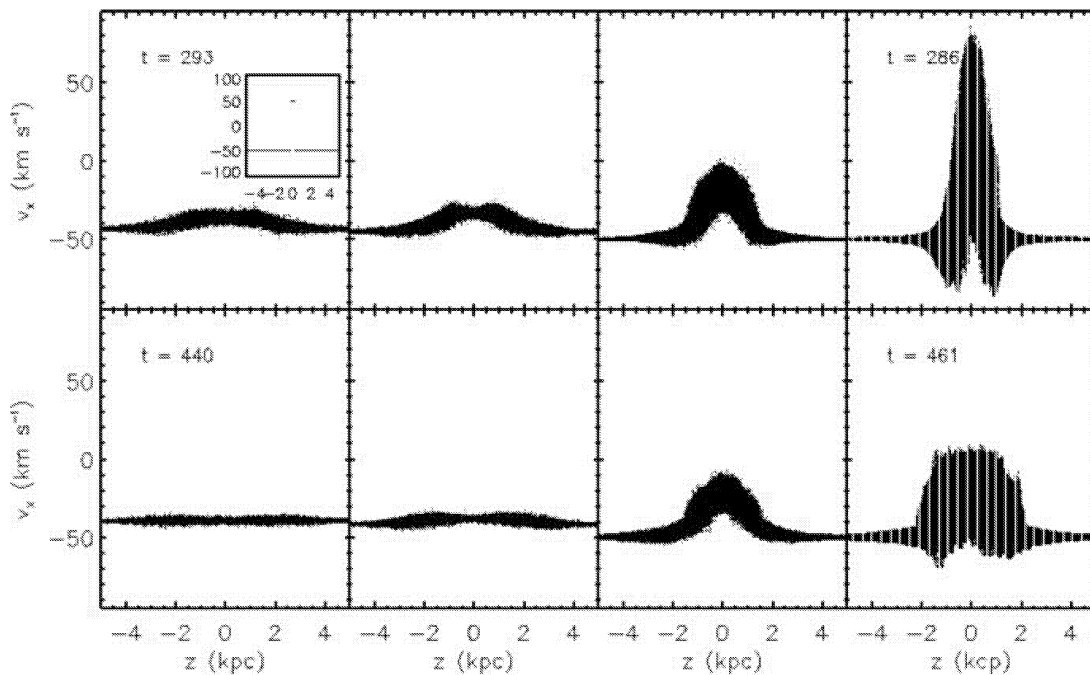


Figure 6. The evolution of the velocity profile in the single temperature shear tests. The results from the SPH runs are shown in the three left-hand columns ($(N_{\text{gas}}, N_{\text{ngb}}) = (32^3, 40)$, $(64^3, 40)$ and $(64^3, 320)$ from left to right) and the results from the FD code are shown in the right-hand panels. The top and bottom panels corresponds the outputs at $t = 293$ and 440 Myr for the SPH simulation and $t = 286$, and 461 Myr for the FD simulation, respectively, and an insert in the top left-hand panel shows the initial velocity field.

to simulate gas stripping from a galaxy by the ram pressure of the intracluster medium (ICM) (Quilis, Moore & Bower 2000) and the evolution of a bubble in the ICM (Quilis, Bower & Balogh 2001). We set up the same initial conditions for the shear test on 151^3 cells. This number provides ample resolution and ensures that each cell hosts only one phase initially. Random noise is added to the density in each cell ($\Delta\rho/\rho \leq 0.01$), otherwise nothing will happen.

The evolution of the velocity profile for each simulation is shown in Fig. 6. For the SPH runs employing only 40 neighbours, the velocity shear decays rapidly owing to momentum transfer across the shear boundary. Using 320 neighbours, the transfer of momentum is significantly suppressed. In the FD simulation, the width of the distribution of v_x values at a particular z coordinate reflects large scale turbulence that is not apparent in the SPH runs. The peak velocities are typically larger and the velocities of the layers distant from the contact surfaces remain intact even after five box-crossings of evolution.

By its very nature, SPH is not well-suited to solving problems involving large discontinuities. In the following subsection we will show more vividly how the SPH and FD methods give qualitatively different results regarding turbulence. However, it is instructive to understand the difference between the SPH runs considered above. As we have seen, the hydrodynamical force can be split into two components: pressure gradients and artificial viscosity. The latter depends upon the relative velocity of the fluids and the size of the interacting volume. This boundary layer should be the same for the $(32^3, 40)$ and $(64^3, 320)$ simulations, because $N_{\text{ngb}}/N_{\text{gas}}$ is identical. However, the first and third columns of panels in Fig. 6 provide drastically different results, so we can infer that the pressure gradients must be behind this variation. Fig. 7 shows at early times that these two simulations do lose momentum at a similar rate. The $(64^3, 40)$ run, and its smaller boundary layer, initially slow down less rapidly. As the relative velocity of the gases decreases, the dominant force

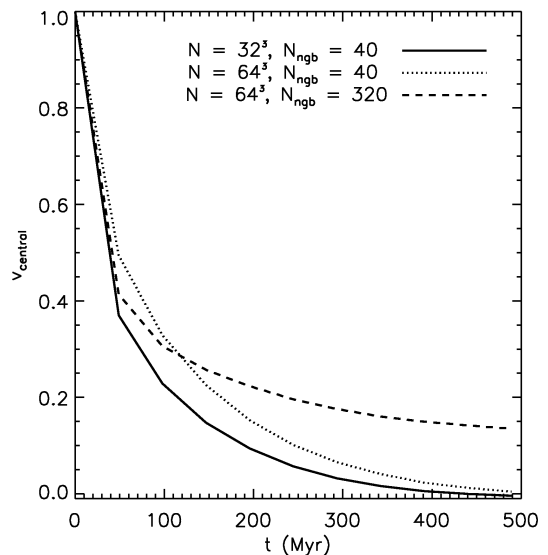


Figure 7. Evolution of the mean x velocity of the cold phase in units where 1 corresponds to the initial velocity and 0 is reached when all shear has gone. Solid, dotted, and dashed lines indicate the shear simulations using $(N_{\text{gas}}, N_{\text{ngb}}) = (32^3, 40)$, $(64^3, 40)$ and $(64^3, 320)$, respectively. At early times, the momentum loss is caused largely by artificial viscosity. As the relative velocity decreases, pressure gradients provide the more important deceleration.

leading to deceleration becomes that coming from pressure gradients. This depends on N_{ngb} , such that more neighbours yield smaller decelerations. Thus, it seems to be noisiness in the SPH smoothing of variables which gives rise to these pressure gradients and a significant proportion of the deceleration. The late time-evolution in

Fig. 7 shows the reduced deceleration of the (64^3 , 320) run relative to the other two. Note that increasing the number of neighbours in SPH calculation significantly slows down the simulation as well as decreasing the mass resolution. Imaeda & Inutsuka (2002) pointed out that density errors in SPH simulations of shear flows can be substantially suppressed by treating particle velocity and fluid velocity separately. However, their method is quite slow and so far only works with a constant smoothing length (Imaeda, private communication).

4.1.2 A two-phase gas

Now that we have seen how SPH behaves when there is a sharp velocity gradient, it is worth investigating the more realistic case of a cold slab of gas moving relative to a hotter medium. To this end, we have recreated initial conditions with the central slab of gas having $T_{\text{cold}} = 10^5$ K and the remaining gas left at $T_{\text{hot}} = 10^6$ K. The sound crossing time for the cold slab (i.e. $0.6 \text{ kpc}/c_s$) is ~ 12 Myr, and ~ 57 per cent of the mass is in the cold phase. This time, when creating the initial conditions, only the temperature of the cold phase and velocities were damped, although a maximum temperature of T_{hot} is also imposed. Simulations were performed using 16^3 , 32^3 , and 64^3 particles.

Fig. 8 shows the densities, pressures, and temperatures of the particles in the relaxed initial conditions using $N = 32^3$ particles. It is apparent that the SPH density and pressure deviate from the analytical curves near the boundary. The presence of features like these is inevitable with SPH (see Pearce et al. 1999; Ritchie & Thomas 2001). Hot particles near to the cold dense slab overestimate their densities and hence pressures. This causes the hot gas to expand away from the dense region, adiabatically cooling in the process, and creating a gap between the two phases which is clearly visible in Fig. 9. This figure also shows that the cold slabs are divided into layers, the number of which depends upon the size of the SPH smoothing length.

We now switch on the shear flow as before. The boundary layer is now unstable to the Kelvin–Helmholtz instability (Landau & Lifshitz 1987). The presence of a fixed gravitational potential can in principle stabilise long wavelength modes but for our configuration this effect can be largely ignored. The left-hand column of panels in Fig. 9 shows the evolution of the x – z projections of particles in the $N = 16^3$ simulation. It is apparent at later times that the cold slab is breaking apart. Instabilities are clearly visible at $t = 98$ Myr. At $t = 342$ Myr an underdensity can be seen at $(x, y) \sim (4.5, 2)$. This subsequently grows and the cold phase at $t = 489$ Myr no longer looks like a slab. This is confirmed in the face-on projections shown in Fig. 10. Note that while the morphology of the phases changes, the membership of each phase is constant with cold particles remaining cold and hot ones hot. This contrasts starkly with the behaviour of the FD simulation, shown in the right-hand column of panels in Fig. 9, where the turbulence mixes the phases at the boundary between them.

In the middle column of panels in Fig. 9, we show the particle distributions in the $N = 32^3$ simulation. The instability appears at $t = 49$ Myr, and then vanishes quickly. No significant evolution is observed in either this run or that with $N = 64^3$, and in neither case do the two phases mix at all. Rerunning the $N = 32^3$ simulation with a cold gas slab of width 0.4 kpc , rather than 0.6 kpc , does produce holes. These runs lead us to conclude that the holes seen here, and also in the simulations of disc formation, were formed due to numerical artifacts. To avoid the formation of holes, the cold phase

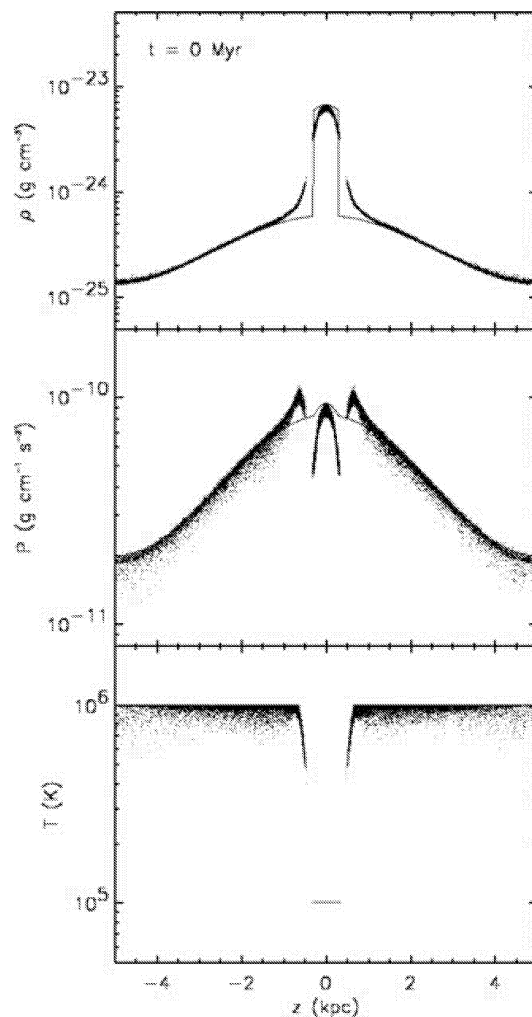


Figure 8. Densities (top), pressures (middle), and temperatures (bottom) of the particles in the relaxed initial conditions with $N = 32^3$. The target density and pressure calculated from the external potential are given by the solid lines.

must contain enough particles. This is a more important consideration than the number of SPH neighbours being used. It is quite hard to maintain enough cold gas disc particles to prevent hole formation in galaxy formation simulations, especially when star formation is included.

One consequence of hole formation is shown in Fig. 11, where the evolution of the mean velocity of the cold phase in the x -direction is traced for each SPH simulation. As there is no mixing of the two phases, the evolution of the mean velocity is equivalent to the evolution of the momentum of the cold slab. The momentum of all the gas is well conserved, so any change in the velocity of the cold phase should be regarded as the result of a momentum transfer with the hot phase. There is a resolution dependence of the size of the initial deceleration when the slab is perturbed by the Kelvin–Helmholtz instability. We have confirmed that this deceleration is caused by the pressure gradient force rather than the artificial viscosity. After the initial deceleration, the slabs lose their momentum at an almost constant rate, where the acceleration from pressure gradients and artificial viscosity are both important. For the lowest resolution run, an additional feature in the momentum evolution can now be seen at $t \sim 350$ Myr. This corresponds to the epoch when the hole forms

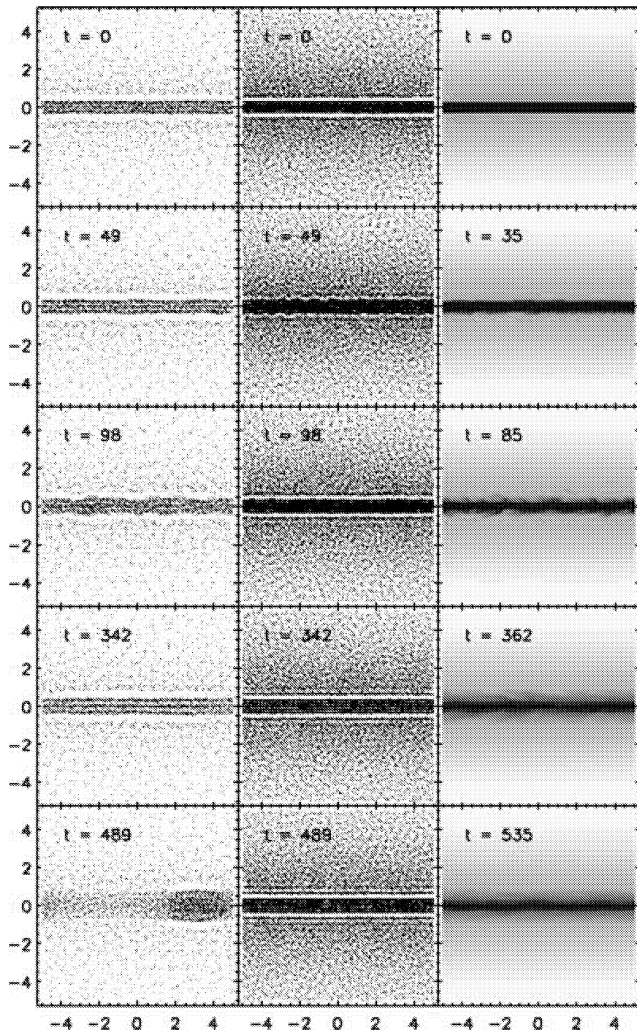


Figure 9. The evolution of the x - z projections of particles in the shear simulations using 16^3 SPH particles (left-hand column), 32^3 particles (middle column) and gas density in the FD code (right-hand column).

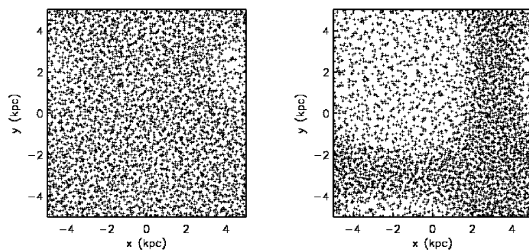


Figure 10. The x - y projections of particles at $t = 342$ (left) and 489 Myr (right) in the shear simulation using 16^3 particles.

in this run and ram pressure from the hot intra-hole gas leads to an extra deceleration of the cold material. Such an effect is not evident in the simulations using 32^3 and 64^3 particles. Their results nearly converge, apart from the initial deceleration, although presumably not to a realistic answer given that the SPH scheme suppresses any phase mixing.

In Table 1 we show the hydrodynamic acceleration parallel to the x -direction acting on the cold phase in each run at $t = 489$ Myr. As expected, the cold slab in the $N = 64^3$ run receives weaker deceleration

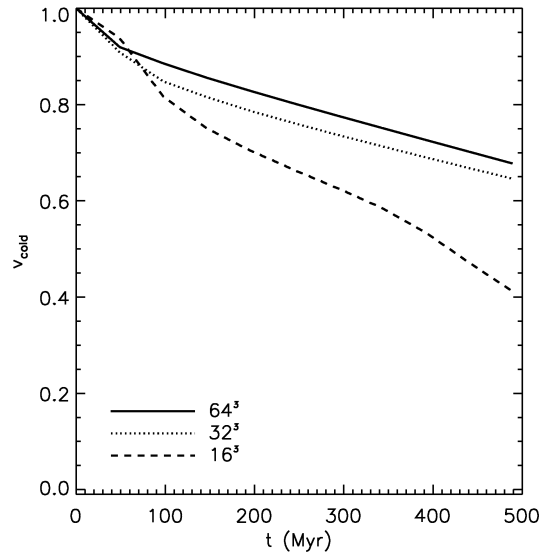


Figure 11. Evolution of the mean x velocity of the cold phase in units where 1 corresponds to the initial velocity and 0 is reached when all shear has gone. Solid, dotted, and dashed lines indicate the shear simulations using 64^3 , 32^3 , and 16^3 particles, respectively. The inflection point at $t \approx 350$ Gyr for the lowest resolution run results from hole formation in the cold slab and ram pressure becoming important in enhancing the momentum loss.

Table 1. Hydrodynamic acceleration parallel to the x -direction acting on the cold phase in each SPH simulation at $t = 489$ Myr. The first column indicates the number of particles in the simulation. The second, third, fourth and fifth columns show the total acceleration, the acceleration from the artificial viscosity, the acceleration from the pressure gradients and the acceleration from the ram pressure respectively. The acceleration is normalized by the velocity of the cold phase. The unit is Gyr^{-1} .

	$(a_x/v_x)_{\text{total}}$	$(a_x/v_x)_{\text{AV}}$	$(a_x/v_x)_{\nabla P}$	$(a_x/v_x)_{\text{RP}}$
16^3	-1.9	-0.21	-1.7	-1.0
32^3	-0.55	-0.35	-0.21	0.035
64^3	-0.59	-0.32	-0.27	-0.011

ation from the artificial viscosity than in the $N = 32^3$ run. Although the cold phase in the $N = 16^3$ run receives the weakest deceleration from the artificial viscosity, we ignore it because the morphology of the cold phase in this run is no longer a slab. Interestingly, the deceleration from pressure gradients is greater in the $N = 64^3$ run than in the $N = 32^3$ run. We also estimate the contribution of ram pressure to the pressure gradient-based deceleration by calculating

$$a_{\text{RP}} = \frac{1}{\rho} \frac{\partial \rho v_x^2}{\partial x} \quad (8)$$

using an SPH gather formulation. In the $N = 16^3$ simulation, half of the deceleration comes from ram pressure, while the contribution of the ram pressure is negligible in other simulations. It proves that the artificial hole formation in the smallest simulation significantly enhances the momentum transfer.

The slabs in $N = 32^3$ and 64^3 receive larger acceleration from the artificial viscosity than the pressure gradients. We have checked, however, that the slabs lose their momentum more quickly only by pressure gradients when we switch off the artificial viscosity, because the lack of the artificial viscosity increases the numerical diffusion and the noisiness in the particle distribution.

4.1.3 Other SPH implementations

While the numerical difficulties caused by sharp boundaries will inevitably impact adversely upon all standard implementations of SPH, it is useful to be aware of the variation in momentum transfer rates within this set of algorithms. We now show the results for two other SPH implementations. The first one employs an arithmetically symmetrized equation of motion and an asymmetric form of the energy equation. This was dubbed ‘energy: asymmetric’ in Springel & Hernquist (2002), produced the best results among the conventional SPH family and has been widely used in galaxy formation (Evrard 1988; Rasio & Shapiro 1991; Navarro & White 1993; Steinmetz & Müller 1993; Haltman & Källander 1997; Thacker et al. 2000). The second SPH variant we choose is one that employs the geometric mean to symmetrise the equation of motion and the energy equation. This formula was proposed by Hernquist & Katz (1989), and was called ‘energy: geometric’ in Springel & Hernquist (2002) where it produced the worst results in their tests. In accordance with Springel & Hernquist (2002), we refer to our default implementation as ‘entropy: conservation’. Note that we regenerate initial conditions for each run using the appropriate SPH variant to generate relaxed initial conditions.

In Fig. 12, we plot the evolution of the mean velocity of the cold slabs in the simulations adopting the above three flavours of SPH. The number of the particles in each simulation is 32^3 . If we assume that better algorithms lose less momentum, then we reach the same conclusion as Springel & Hernquist (2002) despite using a completely different test, namely that ‘entropy: conservation’ is the best and ‘energy: geometric’ is the worst.

4.2 Disc formation in a rotating sphere

We now consider the idealized case of disc formation in a virialized rotating sphere similar to that studied by Navarro & White (1993) and Thacker et al. (2000). The purpose of this exercise is to obtain a quantitative understanding of how the numerical

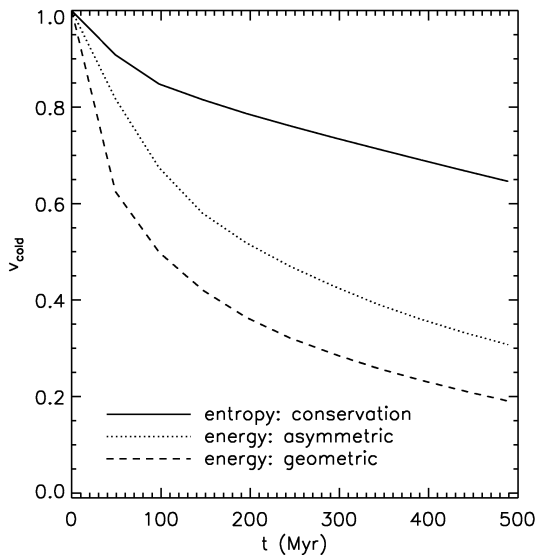


Figure 12. The same as Fig. 11, but for the different implementations of SPH. In each simulation, 32^3 particles are used. The solid, dotted, and dot-dashed lines indicate ‘entropy: conservation’, ‘energy: asymmetric’, and ‘energy: geometric’ implementations, respectively. The solid line here is the same as the dotted line in Fig. 11.

effects studied in the preceding subsections impact upon simulations that are closer to what we expect occurs when galaxies form.

The initial conditions are created by placing particles on a cubic grid with a spherical edge, and perturbing them radially to give a density profile of the form $\rho(r) \propto r^{-1}$. Their velocities are chosen so that the sphere will end up in solid-body rotation around the z -axis; the initial angular momentum J corresponds to a value of the spin parameter, $\lambda = J|E|^{1/2}/(GM^{2.5}) \sim 0.1$, where E is the total energy of the system. The initial radius of the sphere is taken to be 100 kpc, and its mass $10^{12} M_{\odot}$, giving a free-fall time from the edge of the system of about 524 Myr. A baryon fraction of 0.1 is assumed and equal numbers of dark matter and gas particles are used.

In order to prevent the disc from becoming Toomre unstable, we impose a high minimum temperature $T_{\min} = 10^5$ K. This floor is still well below the virial temperature of the system $T_{\text{vir}} \sim 3 \times 10^6$ K, and has the additional benefit of softening the Jeans condition given in equation (4).

The simulation is allowed to evolve for 1.25 Gyr without cooling to let the hot gas reach equilibrium in the halo. Then radiative cooling is switched on [using the cooling function computed for collisional ionization equilibrium by Sutherland & Dopita (1993) assuming a primordial mix of H and He, and $\mu = 0.59$] and the system is followed until $t = 8$ Gyr.

4.2.1 Cooling only simulations

We first perform a series of cooling only (no star formation) simulations using $N_{\text{gas}} = 1736, 5544, 15\,408, 28\,624$ and $44\,442$ SPH particles. The same gravitational softening, $\epsilon = 2$ kpc, is adopted for gas and dark matter particles for the simulation using 2×1736 particles. Softening lengths for other simulations are chosen as $\epsilon = 2 \times (1736/N_{\text{gas}})^{1/3}$ kpc. The SPH smoothing length is allowed to decrease to $h_{\min} = 0$ in all runs because this choice results in better numerical convergence. Here, the relatively high temperature floor (10^5 K) obviates the need to impose a minimum smoothing length.

‘Cold gas’ is defined as gas that with a temperature lower than 1.3×10^5 K. The top panel of Fig. 13 shows the evolution of the cold gas disc mass. Higher resolution allows higher central gas densities, so the better resolved runs have higher cooling rates in the first ~ 1 Gyr. After this time, the simulations using more than $\sim 15\,000$ gas particles create almost identical disc masses, and that with 5544 SPH particles is only a few per cent lower.

The evolution of the specific angular momenta of the cold gas discs, shown in the lower panel of Fig. 13, is more varied. As the cooling is not calculated correctly in the simulation with 1736 gas particles, we will ignore this case. Among the remaining simulations, there is a monotonic increase of angular momentum with increasing resolution and the evolution converges at $N_{\text{gas}} = 28\,624$. In all cases, the specific angular momenta are decreasing functions after $t = 3$ Gyr for all the simulations that resolve the cooling adequately, despite the monotonic increase of specific angular momentum with radius when the cooling is switched on. As the total angular momentum of the gas is well conserved, this implies that there is some transfer within the gas.

In summary, for this particular test, at least 5000 total gas particles are needed before the disc mass is well determined, while more than 25 000 are required to estimate the angular momentum of the disc

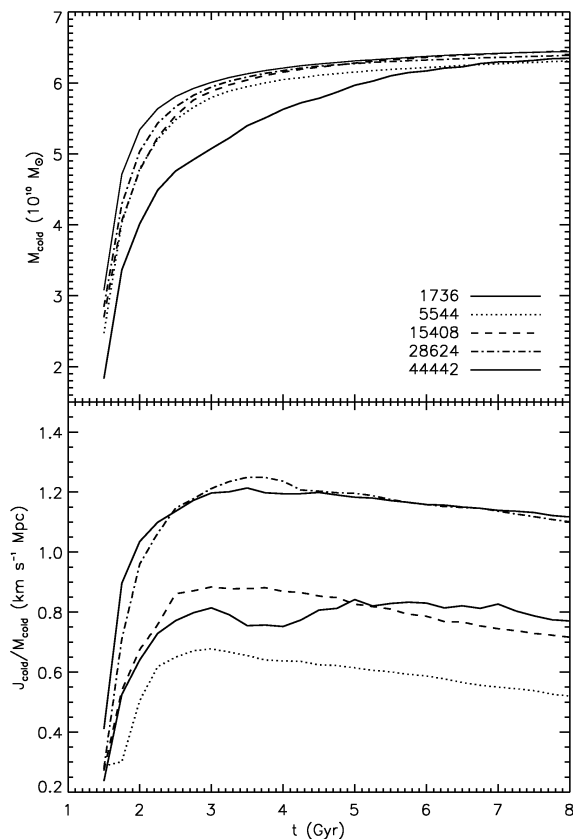


Figure 13. Evolution of the cold gas discs in the cooling-only simulations. The solid, dotted, dashed, dot-dashed and triple-dot-dashed lines denote simulations that employ $N_{\text{gas}} = 1736, 5544, 15408, 28624$, and 44442 , respectively. The upper panel shows the mass of the cold gas disc as a function of time (integrated cooling rate). The lower panel shows the specific angular momentum of the cold gas disc.

reliably. Only about 60 per cent of these particles actually end up in the disc itself.

4.2.2 Simulations with star formation

As seen in Section 3, the specific angular momentum of a cold gas disc depends strongly on the number of particles it contains. Thus, including star formation with an algorithm that decreases the number of cold gas particles should exacerbate the loss of angular momentum from the cold gas disc. We now present simulations similar to those of the previous section, but also employing the ‘conversion’ star formation scheme. A lower threshold density of $\rho_{\text{th}} = 10^{-25} \text{ g cm}^{-3}$ was adopted, because the cold gas disc is more diffuse than in the cosmological simulation as a result of the higher minimum temperature allowed for the cold gas (10^5 K). We only show results from simulations for which a minimum smoothing length was not imposed, and omit both the lowest resolution simulation, in which cooling was not properly followed, and the $N_{\text{gas}} = 28624$ simulation, which is abased by star formation to the low-resolution family. A simulation using $N_{\text{gas}} = 130536$ is added to study resolution effects.

In Fig. 14, we plot the integrated cooling and star formation rates, the mass of the cold gas disc, and the specific angular momentum of the cold gas disc. The cooling rates are very similar to those in the cooling-only simulations, so star formation does not greatly

affect the cooling rate when a halo contains a sufficient number of gas particles ($N_{\text{gas}} \geq 5000$). At the end of the simulation there is a factor of 2 difference in the cold gas masses as the resolution is varied. However, this is a small fraction of the baryonic mass, with only 48, 94, 794, and 2192 cold gas particles remaining in the $N_{\text{gas}} = 5544, 15408, 44442$, and 130536 simulations, respectively.

As was seen in the cooling-only simulations, the decline of the specific angular momentum of the cold gas discs starts from $t \sim 3 \text{ Gyr}$ when the rapid accretion of cold gas finishes. These decreases are much stronger than those in the cooling-only simulations, because the cold gas discs now contain fewer particles. Despite this, the two highest resolution simulations still manage to produce reassuringly similar results. Compared with the cooling-only runs, the values of the specific angular momenta of the cold gas discs are significantly higher. This is because the low angular momentum cold gas is preferentially creamed off and converted into stars.

The lower panel in Fig. 15 shows the final specific angular momenta of the stars as a function of their formation time. The overall shape of these curves reflects the angular momentum evolution in the cold gas, albeit shifted downwards by ~ 30 per cent. The declining stellar specific angular momentum at late times implies that there would be outside-in disc formation, i.e. older stars have larger angular momentum. The outside-in disc formation found by Sommer-Larsen et al. (2002) might be explained by this process. It is crucial to obtain a numerically robust estimate of the angular momentum evolution of the cold gas before the stellar population distribution in the disc can be reliably studied.

The evolution of the total stellar specific angular momentum is shown in the upper panel of Fig. 15. These results are dominated by the bulk of the stars which form in the first few Gyr after cooling is switched on. The small differences in the cold gas angular momenta for the two highest resolution runs at these early times are sufficient to imprint similar-sized differences in the final stellar angular momenta. It should be noted that the specific angular momenta of the stellar discs would depend on the resolution even if the cold gas discs had exactly the same specific angular momenta. The reason for this is that higher resolution enables higher density regions to be resolved at large radii. In addition, a shorter gravitational softening length gives higher gas density for a given surface gas density. Consequently, higher resolution allows higher angular momentum gas to form stars. In order to achieve numerical convergence, we should include self-regulated star formation tuned to give the surface density of the star formation rate as a function of the surface gas density (Gerritsen & Icke 1997; Springel & Hernquist 2003, see also Yepes et al. 1997; Hultman & Pharisyn 1999) as the observations suggest (Kennicutt 1998). Carraro, Lia & Chiosi (1998) and Buonomo et al. (2000) have pointed out that inclusion of feedback processes, for example, Type Ia and II supernovae, stellar winds, and ultraviolet radiation from massive stars, has a significant impact on the evolution of model galaxies. Including feedback processes is, however, beyond the scope of this paper.

Fig. 16 shows the distribution of the cold gas particles in the star formation runs with $N_{\text{gas}} = 15408$ and 130536 . In the $N_{\text{gas}} = 15408$ simulation, the cold gas disc has some small holes at $t = 3 \text{ Gyr}$. At $t = 6 \text{ Gyr}$ the holes have become large and finally the cold gas disc shrinks to the centre at $t = 8 \text{ Gyr}$. The evolution in the $N_{\text{gas}} = 130536$ simulation shows the same trend, but the disc is much smoother. At $t = 3 \text{ Gyr}$ the disc has beautiful spiral arms, and then some small holes appear at $t = 6 \text{ Gyr}$. The final disc is much more extended than that in the lower resolution simulation, but it has acquired unphysically large holes.

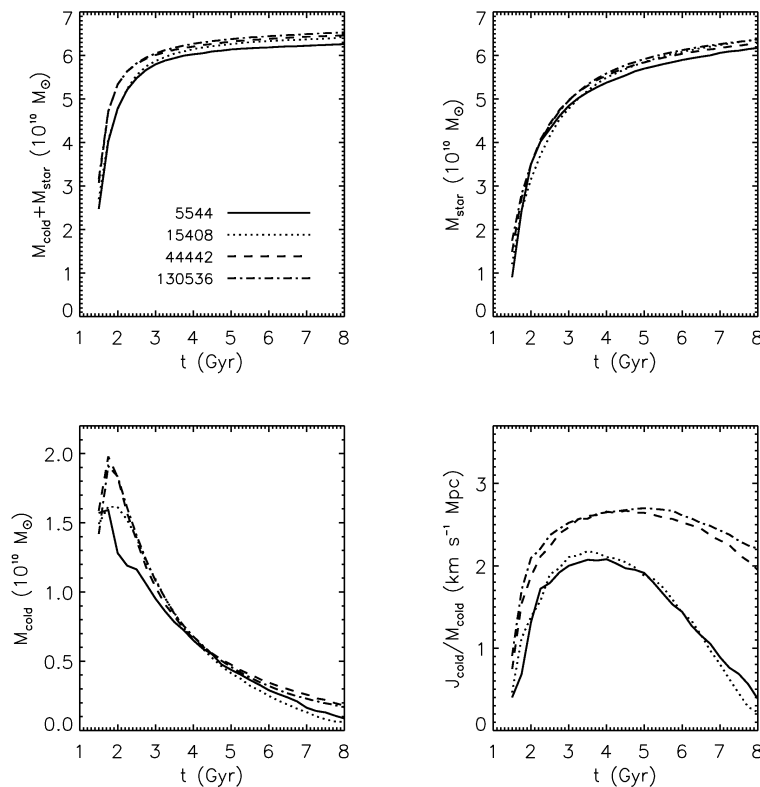


Figure 14. Evolution of the cold gas discs in the simulation with star formation. The integrated cooling rate, the integrated star formation rate, the remaining cold gas mass, and the specific angular momentum of the remaining cold gas are plotted in the upper left-hand, upper right-hand, lower left-hand and lower right-hand panels, respectively. The solid, dotted, dashed and dot-dashed lines indicate the simulations with $N_{\text{gas}} = 5544, 15\,408, 44\,442$, and $130\,536$, respectively.

Table 2 displays the hydrodynamic torques acting on the cold gas discs at $t = 5.5$ Gyr, both in the cooling-only and star formation series. We find that the cold gas discs in the simulations with star formation received much stronger negative torques compared with the cooling-only runs with the same initial N_{gas} . Part of the reason for this is that the torque from the artificial viscosity has a strong dependence on the number of cold gas particles. However, the contribution to the torque from the pressure gradients is also significantly larger in the star formation runs. This is due to ram pressure caused by the creation of holes once enough gas particles have been converted to stars. In the $N_{\text{gas}} = 130\,536$ simulation, this torque becomes stronger than that caused by the artificial viscosity. Thus, even in this best-resolved simulation, the cold gas disc is depleted to an extent where resolution-dependent holes are formed and resolution-dependent fractions of the angular momentum are lost.

5 DECOUPLING THE COLD PHASE FROM THE HOT PHASE

In the previous sections we have seen that the angular momentum transfer from the cold gas to the hot halo gas is mainly caused by numerical problems which are intrinsic to the SPH technique. The collapsing rotating sphere test in the previous section reveals that the problem becomes worse when star formation is included. The reason for this is as follows. Star formation decreases the number of particles in the cold gas disc causing the disc to become thinner. We had found in the preceding section that a disc is prone to develop holes when the number of particles in it is not sufficient. Once these

holes appear, ram pressure between the hot and cold gas phases becomes important and a rapid loss of angular momentum from the cold gas ensues.

It is interesting therefore to see what happens when we inhibit the angular momentum transfer from cold gas to hot gas in simulations of galaxy formation. This can be achieved in a drastic way by decoupling the cold and hot phases. Pearce et al. (1999) proposed a decoupling technique whereby the contribution to the density of the hot gas particles from the cold gas particles is explicitly ignored. This has the effect of suppressing the overcooling of the hot gas that otherwise results. In this scheme hot and cold particles nonetheless interact through mutual hydrodynamical forces. Our approach is more radical: hot and cold particles do not interact at all except through gravity. The cold and hot phases are treated as independent fluids. Our approach is quite similar to the multi-phase model proposed by Semelin & Combes (2002) in which they represents a warm phase by SPH particles and the interstellar medium (ISM) by sticky particles and do not allow the ISM to interact with ambient gas hydrodynamically. While clearly we miss some real physics as a result of such decoupling, the physics that we miss cannot be modelled properly using SPH anyway as we have shown. In the following subsections we show simulations of disc formation adopting this decoupling technique.

5.1 Disc formation in a rotating sphere

The technique of decoupling is appropriate in situations in which the pressure from the hot gas is unimportant in confining the cold gas component and when the pressure at the midplane of the cold gas

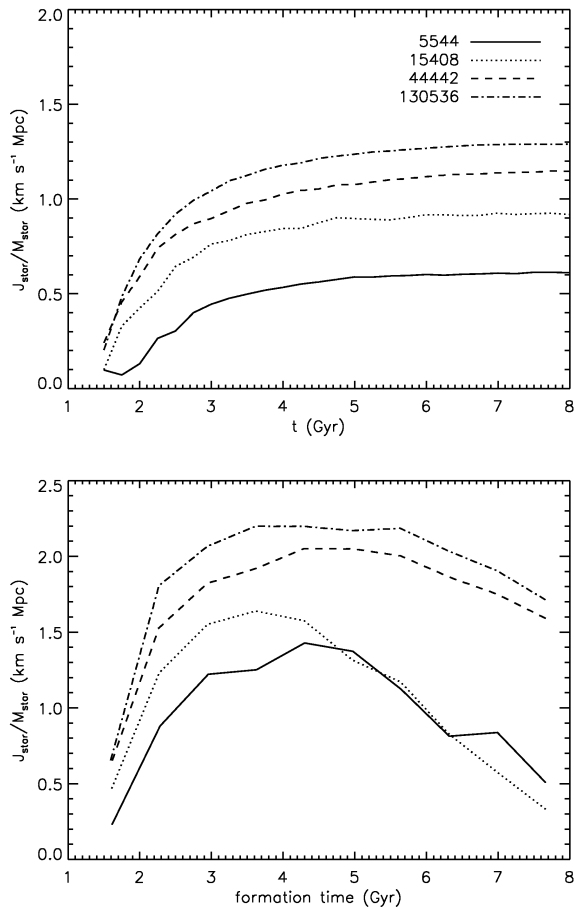


Figure 15. Evolution of the stellar discs angular momentum (upper panel) and formation time-angular momentum distributions in the stellar discs at $t = 8$ Gyr (lower panel). The solid, dotted, dashed and dot-dashed lines indicate the simulations with $N_{\text{gas}} = 5544, 15\,408, 44\,442$ and $130\,536$, respectively.

disc is sufficiently greater than the external pressure on the contact surfaces. In such a situation, the self-gravitating gas disc can be a good approximation. We now present simulations including star formation, which are similar to those discussed in Section 4.2.2 and illustrated in Figs 14–16.

Fig. 17 shows the evolution of the cold gas disc. The integrated cooling rates are almost the same as in Fig. 14. The stellar mass is also similar to that in the normal simulation, but more mass remains as cold gas (about a factor of 2). The evolution of the specific angular momenta of the cold gas discs are quite different from those in Fig. 14. Apart from the lowest resolution simulation, the simulations no longer show a decrease in the specific angular momentum as a function of time. Even the lowest resolution simulation shows a decline which starts much later and the disc ends up with much larger specific angular momentum than in the normal SPH simulation. This proves that most of the angular momentum loss from the cold gas disc is due to the hydrodynamic interaction with the ambient hot gas, which cannot be dealt with adequately by SPH. A resolution dependence is still present, because the accreting gas can have large velocity shears before it reaches the temperature below which it becomes decoupled from the hot gas. We have also investigated the torque that causes the decline of the angular momentum of the cold gas disc in the lowest resolution simulation. We find that most of the negative torque is coming from the gravitational interaction with

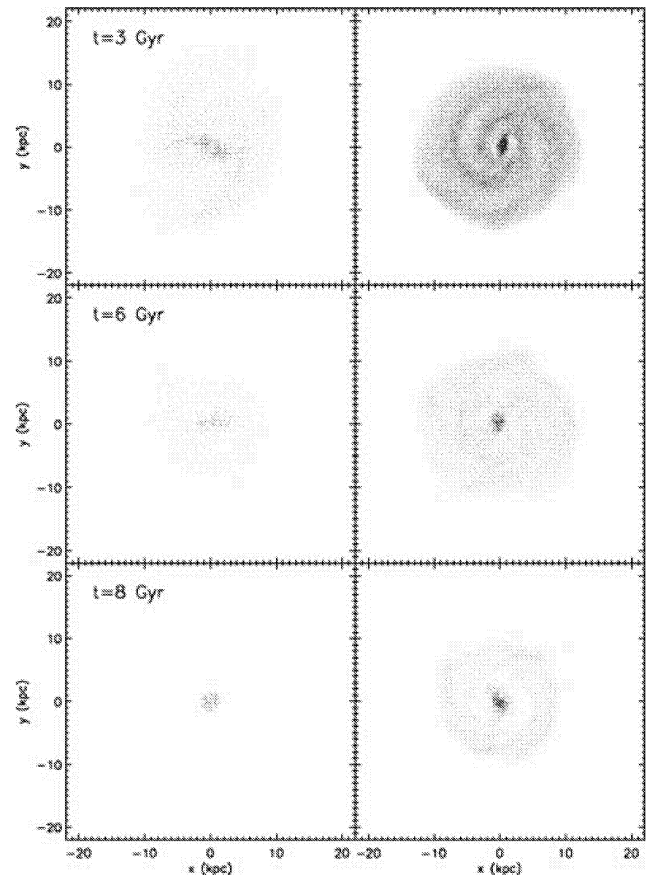


Figure 16. Distribution of cold gas in the star formation runs, $N_{\text{gas}} = 15\,408$ (left) and $130\,536$ (right). The grey-scale is coded by the three-dimensional gas density.

Table 2. Hydrodynamic torques acting on the cold gas discs parallel to the angular momenta of cold gas discs at $t = 5.5$ Gyr. The second, third, and fourth column show the total hydrodynamic torques, the hydrodynamic torques from the pressure gradient force, and the hydrodynamic torques caused by the artificial viscosity. The torques are normalised by the angular momenta. The unit is Gyr^{-1} .

N_{gas}	$(\tau_{\text{cold}}/J_{\text{cold}})_{\text{hydro}}$	$(\tau_{\text{cold}}/J_{\text{cold}})_{\nabla P}$	$(\tau_{\text{cold}}/J_{\text{cold}})_{\text{AV}}$
15 408 (no SF)	−0.048	−0.017	−0.031
28 624 (no SF)	−0.035	−0.013	−0.021
44 442 (no SF)	−0.033	−0.015	−0.017
15 408 (SF)	−0.19	−0.11	−0.079
44 442 (SF)	−0.069	−0.028	−0.042
130 536 (SF)	−0.067	−0.044	−0.023

stellar and dark matter particles. We conjecture that this is because the density distributions of the cold gas disc and the stellar disc are not smooth enough to prevent angular momentum transfer due to tidal torques.

In Fig. 18, we show the face-on views of the cold gas discs in the simulations using $N_{\text{gas}} = 15\,408$ and $130\,536$. Both produce smooth extended cold gas discs without any holes. The main difference due to resolution is in the three-dimensional density of cold gas particles and in the ability to resolve spiral arms. These are direct consequences of the differences in the spatial resolution of gravity and mass resolution in the SPH.

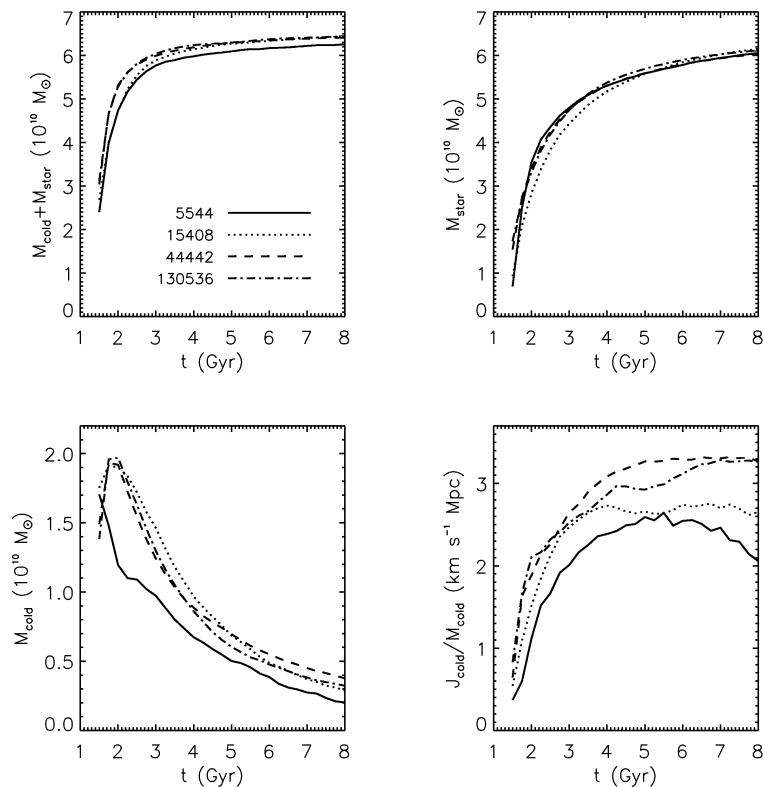


Figure 17. The same as Fig. 14 but with the decoupling.

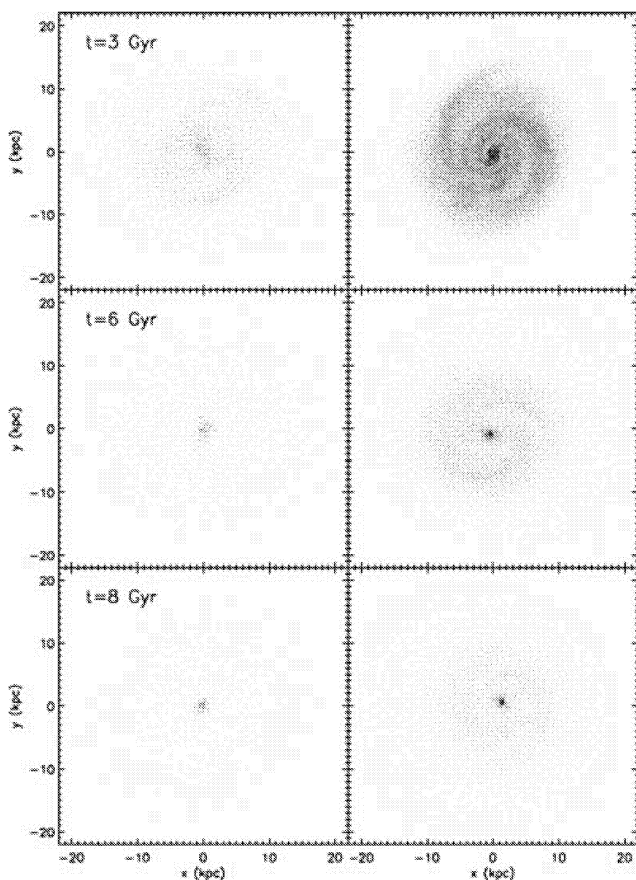


Figure 18. The same as Fig. 16 but with the decoupling.

The evolution of the stellar discs and their age-angular momentum distribution at $t = 8$ Gyr are presented in Fig. 19. Except for the lowest resolution simulation, the angular momentum evolution shows better convergence than in the normal SPH simulations. The reason why the stellar disc in the $N_{\text{gas}} = 15\,408$ simulation has larger specific angular momentum than that in the $N_{\text{gas}} = 44\,442$ simulation is as follows. Although the cold phase is decoupled from the hot phase, angular momentum transfer to the hot gas during accretion before the gas temperature has reached the decoupling threshold (1.3×10^5 K; see Section 4.2.1) is still allowed. Consequently, the lower resolution simulation produces a lower angular momentum cold gas disc. Because the local star formation rate is a function of density and we impose a threshold density for star formation, the low angular momentum of the cold gas disc does not always result in a lower angular momentum for the stellar disc. Higher angular momentum gas particles are often not dense enough to be eligible for star formation. Thus, the angular momentum transfer that brings such gas particles to the inner disc where the gas particles can form stars sometimes produces a higher angular momentum stellar disc. The increasing resolution is also likely to increase the angular momentum of the stellar disc, because higher mass resolution allows fragmentation to be resolved in less dense environments. As a result, the high angular momentum gas particles that cannot form stars in a low-resolution simulation are allowed to form stars if they reside in the dense structures like spiral arms that are resolved with higher resolution (see Fig. 18).

The above complex picture also provides a reasonable explanation for the fact that, at the highest resolution, the stellar disc in the normal SPH simulation (Fig. 15) has a slightly higher angular momentum than in the simulation with decoupling (Fig. 19), despite the fact that the angular momentum of the cold gas disc in the normal SPH simulation is lower than in the simulation with decoupling. The

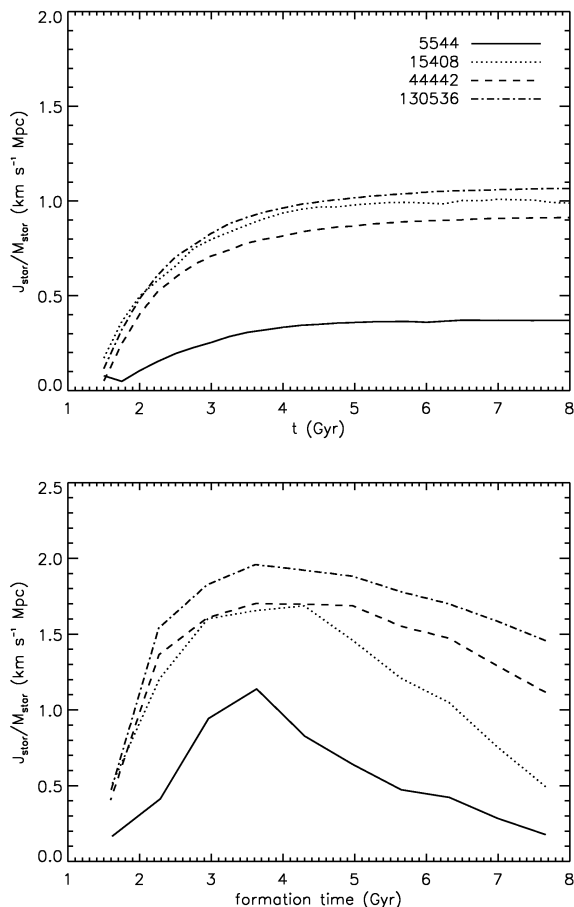


Figure 19. The same as Fig. 15 but with decoupling.

angular momentum transfer from the cold gas makes more cold gas particles eligible to form stars and the holes in the cold gas disc enhance the density of the cold gas disc at large radii. Of course, the pressure from the hot gas also enhances the density and thus the star formation rate all over the disc, but, as we have seen, this process cannot be modelled appropriately by SPH.

The age-angular momentum distribution exhibits the outside-in disc formation feature again, although this is weaker than in the standard SPH simulation. This is not surprising because the star-forming region shrinks when the surface density of the cold gas disc is reduced by star formation. However, as we mentioned above, higher resolution allows stars to form in the outskirts of the disc even when the surface gas density becomes quite low. Hence the outside-in feature becomes weaker with increasing resolution. Even though the resolution limits for the $N_{\text{gas}} = 44\,442$ and $130\,536$ simulations (equation 4) are far below the threshold density for star formation ($\rho_{\text{th}} = 10^{-25} \text{ g cm}^{-3}$), the age-angular momentum distributions do not converge. Self-regulated star formation may remove this resolution dependence as we discussed previously. We will test this in future work.

5.2 Cosmological simulations

Finally, we present cosmological simulations adopting the decoupling of the cold and hot phases. In this case, we allow warm gas ($3 \times 10^4 < T < 5 \times 10^5 \text{ K}$) to interact with both the cold and hot phases so that the simulations do not fail when there are too few

cold gas particles to perform the SPH calculation. All conditions are the same as the simulations presented in Section 3 except for the decoupling between the hot and cold phases.

In Fig. 20, we show the redshift evolution of the cold gas discs in the decoupling simulations. As in Section 3, we adopt two star formation schemes, ‘conversion’ and ‘spawning’. The distributions of the cold gas particles are quite different from those in the standard SPH simulations (see Figs 1 and 2). In the standard SPH simulations, most of the cold gas particles are in the filaments and the remaining regions are almost empty. Now the galaxies have smooth, extended cold gas discs. These gas discs have spiral arms instead of filaments. Because the cold gas particles have a temperature $\sim 10^4 \text{ K}$, which is one order of magnitude smaller than the lower limit in the idealized simulations of Section 4, the cold gas discs are much thinner. This makes the problems encountered in the shear tests more serious. Consequently, the cold gas disc will have an unphysical morphology because of numerical effects *unless* we decouple the cold gas from the hot halo gas. Note that the smooth density distribution of the cold gas disc significantly decreases angular momentum transfer due to tidal torques as well.

Fig. 21 shows the specific angular momenta of the cold gas discs, the integrated cooling rates, and the integrated star formation rates in the galaxies as functions of time. The results from the standard SPH simulations (Fig. 3) are also plotted for reference. Now, with decoupling, the specific angular momenta of the cold gas discs become monotonically increasing functions of time. There is a small difference between the specific angular momenta of the cold gas discs in the two decoupling simulations. This might be because the cold gas disc in the spawning case is less affected by the angular momentum transfer between the cold gas and the warm gas, although we cannot find any significant difference in the hydrodynamic and tidal torques in these two simulations. To decide whether the high specific angular momentum of the cold gas disc in the spawning run is the result of the larger number of cold gas particles or a side-effect of the multi-mass SPH imposed by this star formation prescription, we would have to perform another conversion simulation with a larger number of the SPH particles, leaving all other conditions unchanged. In this paper we do not perform this test because it would require a much larger number of particles in order to satisfy the Jeans condition (equation 4) beyond the threshold density for star formation.

The cooling rates and the star formation rates are almost the same between the two decoupling simulations, and they are higher than in the standard SPH simulations. This proves that the numerical angular momentum feedback puffs up the hot halo gas and the cooling rate is reduced in the standard SPH simulations. Because this effect was not observed in the idealized simulations, we conclude that as the temperature of the cold gas disc becomes lower, the numerical angular momentum transfer becomes more problematic.

To find out how the angular momentum transfer affects the stellar disc, we plot the evolution of the specific angular momenta of the stellar discs and the age-angular momentum distributions at $z = 0$ in the decoupling and standard SPH simulations in Fig. 22. Interestingly, except for the standard conversion simulation, all the other simulations show similar evolution of the specific angular momentum of the stellar discs. On the other hand, except for the standard spawning simulation, all the simulations produce similar results for the age-angular momentum distributions. These may be just a coincidence. Because we impose a relatively high density threshold as a star formation criterion, only cold gas particles that have small angular momenta can form stars and thus the threshold density determines the angular momenta of the stellar discs. It makes the specific

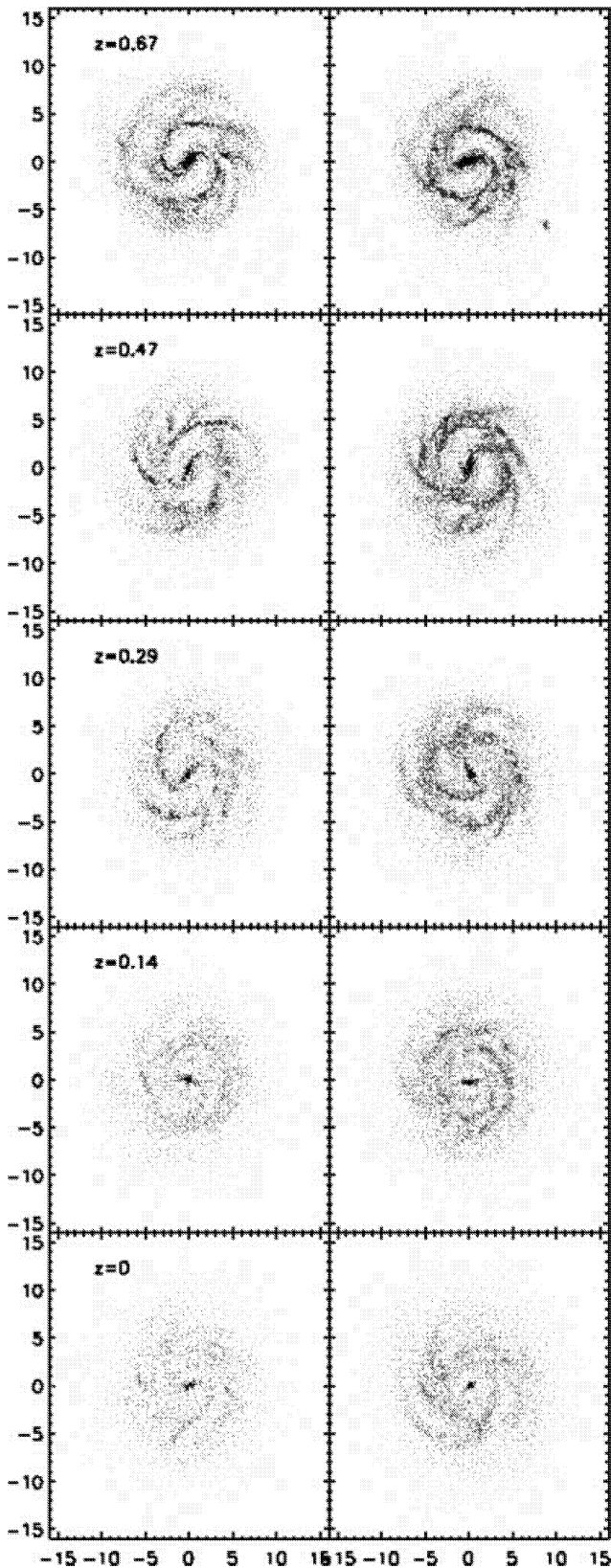


Figure 20. Face-on views of the distribution of cold gas. The left-hand panels show the galaxy in the simulation with decoupling and the ‘conversion’ star formation prescription and the right-hand panels for the simulation with decoupling and the ‘spawning’ star formation prescription. The length is in units of h^{-1} kpc.

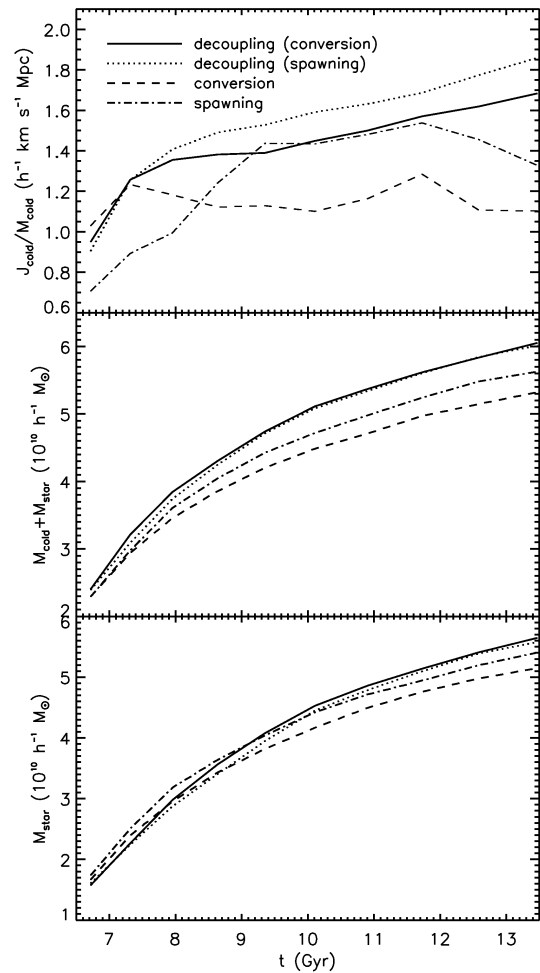


Figure 21. Evolution of the galaxies. The top, middle and bottom panels present the specific angular momenta of the cold gas discs, the integrated cooling rates and the integrated star formation rates, respectively. The solid and dotted lines indicate the decoupling simulations with the conversion and spawning star formation recipes, respectively. The results from the standard SPH simulations are also shown by the dashed (conversion) and dot-dashed (spawning) lines for reference.

angular momentum evolution of the stellar discs almost independent of those of the cold gas discs.

In the standard SPH simulation with the conversion star formation prescription, the formation of holes in the cold gas disc results in the cold gas being swept out to form a dense ring at large radius at high redshifts (see the top left-hand panel of Fig. 2). Gas particles that have large angular momenta can form high angular momentum stars in this ring. On the other hand, in the standard spawning simulation, the gas disc has a large ring at low redshift (see the bottom right-hand panel of Fig. 2). From this ring, the high angular momentum population stars of age ~ 2 Gyr are born. As these holes are numerical artifacts, as we showed in the shear tests, the large angular momentum of the stellar disc and the high angular momentum population in the standard SPH simulations are numerical artifacts as well. If the gas disc is puffed up by some feedback processes and if we choose a lower threshold density for star formation, the simulations with and without decoupling would produce different results as in the case of the idealized simulations with the temperature floor at $T = 10^5$ K. The idealized simulations and the cosmological simulations presented in this paper suggest that the angular momentum transfer

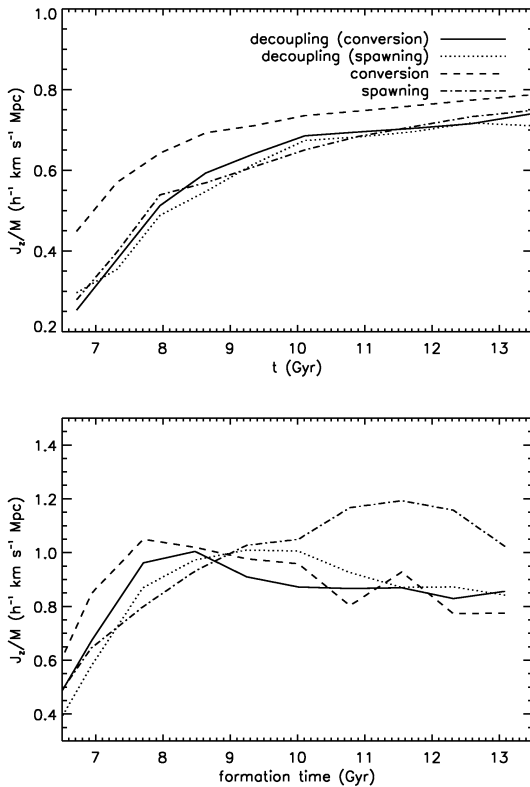


Figure 22. Evolution of the specific angular momenta of stellar discs as a function of time and the age-angular momentum distributions of stars at $z = 0$. The solid, dotted, dashed and dot-dashed lines indicate the decoupling simulations with conversion and spawning star formation and the standard SPH simulations with conversion and spawning star formation, respectively.

from the cold gas disc sometimes results in too large and sometimes too small angular momentum of the stellar disc depending on the resolution and the modelling of the ISM and star formation. It thus must depend on the modelling of feedback as well.

6 SUMMARY AND DISCUSSION

We have found in a cosmological SPH simulation that a disc of cold gas breaks up into filaments and there is a significant transfer of angular momentum from the cold gas disc to the ambient hot halo gas. The dominant contribution to the hydrodynamical torque between the cold and hot phases comes from the pressure gradient forces and not from the artificial viscosity. The hot gas is puffed up by this angular momentum ‘feedback’ and this, in turn, can affect the cooling rate.

By using simple shear tests, we find that SPH cannot correctly solve problems where there are strong shear flows. When a dense cold gas sheet is moving in ambient diffuse hot gas, the gas sheet receives strong negative acceleration due to pressure gradients and artificial viscosity. By varying the number of neighbouring particles involved in the SPH smoothing, we find that the deceleration due to pressure gradients is related to the noisiness in SPH variables. Moreover, if the cold gas sheet does not contain a sufficient number of particles, it undergoes hole formation. Ram pressure from the hot gas in these holes leads to further momentum transfer.

The comparison of simulations using SPH and a finite-difference Eulerian code clearly exhibits a shortcoming of the SPH method: SPH does not generate the turbulent mixing of the fluid components

in the shear flow tests that is present with the Eulerian code. Instead, with SPH the fluid velocities change to damp out the shear flow but without any mixing of fluids. This feature of SPH only becomes problematic when there are large velocity gradients. As previous test simulations did not consider such a large shear, SPH has produced promising results. However, as we have shown in this paper, such a large shear can exist in galaxy formation problems where a rotationally supported cold gas disc forms within hot halo gas that is mainly supported by thermal pressure.

The idealized simulations of disc formation in rotating hot gas reveal that this problem has a strong dependence on the resolution. Having star formation in a simulation makes the situation worse by decreasing the number of cold gas particles. If not enough particles are used, the angular momentum of the cold gas disc steeply declines with time. Consequently, the stellar disc forms from the outside to the inside. This process may explain the outside-in formation of disc galaxies found in the simulations by Sommer-Larsen et al. (2002).

One way to avoid these problems is to decouple the cold and hot gas phases. In the simulations with decoupling, the specific angular momenta of the cold gas discs become monotonically increasing functions of time as expected on theoretical grounds. The main difference from the standard SPH simulations is seen in the morphology of cold gas discs. The simulations with decoupling produce smooth extended cold gas discs that do not have any holes. These simulations also reveal that the numerical angular momentum transfer sometimes increases the specific angular momenta of stellar discs and sometimes decreases them, while it always decreases the specific angular momenta of cold gas discs. This strange feature is caused by the density dependence of star formation. Hence, the way in which this problem affects stellar discs is highly dependent on resolution and on the modelling of subgrid physics in the interstellar medium.

We do not believe that the angular momentum transfer that we have identified here is the main explanation for the angular momentum problem in galaxy formation simulations, because the difference in the specific angular momenta of stellar discs between simulations with and without decoupling is not that large, although it seems to depend strongly on the modelling of subgrid physics such as star formation. At higher resolution, the numerical breaking up of cold gas discs is likely to increase the specific angular momentum of the stellar discs by enhancing the cold gas density and hence star formation rate in the outskirts of the discs. Anyway, as long as the cold gas disc suffers spurious angular momentum transfer and has a strange morphology, the properties of the resulting stellar disc are quite unreliable.

The angular momentum transfer rakes up all the cold gas into the star-forming region and spurious fragmentation of the disc induces quite effective star formation in these dense filaments. Consequently, the problem can be much more serious when one investigates the details of simulated galaxies like the cold gas distribution, the hot gas distribution, the distribution of stellar populations, and all observables related to them. The problem may also affect simulations of elliptical galaxies. After the galaxy has exhausted most of its cold gas in, for example, a starburst, newly accreting cold gas is quickly supplied to the centre regardless of its angular momentum (newly accreting cold gas implies the existence of halo gas). The decoupling of the cold and hot gas phases that we have introduced offers the opportunity to investigate the detailed structure of galaxies by avoiding this spurious angular momentum transfer.

However, it seems clear that complex physical processes taking place in the interstellar medium and in the hot halo gas must play a key role in galaxy formation. A code that can solve problems

involving large shear motions, together with the ability to treat a wide dynamic range, is required to study these processes in detail. AMR is an obvious candidate, although it has not yet been widely used in this subject, and thus still needs substantial testing. On the other hand, substantial refinements of SPH have been introduced recently which could prove useful in this context, for example Monaghan (1989, redefined particle velocity by locally averaged velocity), Owen et al. (1998, tensorial smoothing kernels), Ritchie & Thomas (2001, smoothed pressure SPH), Inutsuka (2002, SPH with Riemann solver), Imaeda & Inutsuka (2002, consistent particle velocity with fluid velocity), Kitsionas & Whitworth (2002, adaptive mass resolution) and Springel & Hernquist (2002, conservation of both entropy and energy). We encourage colleagues who have developed and implemented these refinements to perform the shear tests presented in this paper. The implementation by Imaeda & Inutsuka (2002) is particularly interesting as it substantially suppresses spurious density errors in SPH calculations of shear flows.

The phase decoupling technique that we have introduced may be regarded as a crude way of modelling a multi-phase fluid in cosmological simulations and seems to produce much better results than standard SPH. This decoupling seems a reasonable approximation when the disc is self-gravitating and consists of cold gas and stars. As the multi-phase structure of the interstellar medium begins to be resolved in a simulation, this approximation must break down, because the external pressure from halo gas plays a role in confining the hot phase of the interstellar medium. Modelling these processes remains a challenge which may hold the key for realistic simulations of the formation of galactic discs.

ACKNOWLEDGMENTS

We are grateful to Volker Springel for kindly providing the improved version of GADGET. We also thank to Simon White, Lars Hernquist, Peter Thomas, Julio Navarro, Rob Thacker and Richard Bower for their highly useful comments on this work. We acknowledge the financial support from UK PPARC. VQ acknowledges a Royal Society University Research Fellowship. VQ is a Ramon y Cajal Fellow from the Spanish Ministry of Science and Technology and has partial financial support from grant AYA2000-2045.

REFERENCES

- Abel T., Bryan G. L., Norman M. L., 2000, *ApJ*, 540, 39
 Bate M. R., Burkert A., 1997, *MNRAS*, 288, 1060
 Balsara D. W., 1995, *J. Comp. Phys.*, 121, 357
 Buonomo F., Carraro G., Chiosi C., Lia C., 2000, *MNRAS*, 312, 371
 Carraro G., Lia C., Chiosi C., 1998, *MNRAS*, 297, 1021
 Cole S., Lacey C. G., Baugh C. M., Frenk C. S., 2000, *MNRAS*, 319, 168
 Dalcanton J. J., Spergel D. N., Summers F. J., 1997, *ApJ*, 482
 Davis M., Efstathiou G., Frenk C. S., White S. D. M., 1985, *ApJ*, 292, 371
 Eke V. R., Efstathiou G., Wright L., 2000, *MNRAS*, 315, L18
 Evrard A. E., 1988, *MNRAS*, 235, 911
 Evrard A. E., Summers F. J., Davis M., 1994, *ApJ*, 422, 11
 Fall S. M., Efstathiou G., 1980, *MNRAS*, 193, 189
 Frenk C. S., Evrard A. E., White S. D. M., Summers F. J., 1996, *ApJ*, 472, 460
 Gerritsen J. P. E., Icke V., 1997, *A&A*, 325, 972
 Governato F. et al., 2002, preprint (astro-ph/0207044)
 Haardt F., Madau P., 1996, *ApJ*, 461, 20
 Haltman J., Källander D., 1997, *A&A*, 324, 534
 Hernquist L., Katz N., 1989, *ApJ*, 70, 419
 Hultman J., Pharasyn A., 1999, *A&A*, 347, 769
 Imaeda Y., Inutsuka S., 2002, *ApJ*, 565, 501
 Inutsuka S., 2002, *J. Comp. Phys.*, 179, 238
 Katz N., 1992, *ApJ*, 391, 502
 Katz N., Hernquist L., Weinberg D. H., 1992, *ApJ*, 399, L109
 Katz N., Weinberg D. H., Hernquist L., 1996, *ApJS*, 105, 19
 Kauffmann G., White S. D. M., Guiderdoni B., 1993, *MNRAS*, 264, 201
 Kennicutt R. C., 1998, *ApJ*, 498, 541
 Kitsionas S., Whitworth A. P., 2002, *MNRAS*, 330, 129
 Landau L. D., Lifshitz E. M., 1987, *Course in Theoretical Physics: Fluid Mechanics*. Academy of Sciences, Moscow
 Lombardi J. C., Sills A., Rasio F. A., Shapiro S. L., 1999, *J. Comp. Phys.*, 152, 687
 Mo H. J., Mao S., White S. D. M., 1998, *MNRAS*, 295, 319
 Monaghan J. J., 1985, *J. Comp. Phys. Rep.*, 3, 71
 Monaghan J. J., 1989, *J. Comp. Phys.*, 82, 1
 Monaghan J. J., 1997, *J. Comp. Phys.*, 136, 298
 Monaghan J. J., Gingold R. A., 1983, *J. Comp. Phys.*, 52, 374
 Nagashima M., Totani T., Gouda N., Yoshii Y., 2001, *ApJ*, 557, 505
 Navarro J. F., White S. D. M., 1993, *MNRAS*, 319, 619
 Navarro J. F., White S. D. M., 1994, *MNRAS*, 267, 401
 Navarro J. F., Frenk C. S., White S. D. M., 1995, *MNRAS*, 275, 56
 Netterfield et al., 2002, *ApJ*, 571, 604
 Okamoto T., Nagashima M., 2003, *ApJ*, 587, 500
 Owen J. M., Vllumsen J. V., Shapiro P. R., Martel H., 1998, *ApJS*, 115, 155
 Pagels H., Primack J. R., 1982, *Phys. Rev. Lett.*, 48, 223
 Pearce F. R. et al. (The Virgo Consortium), 1999, *ApJ*, 521, L99
 Quilis V., Ibáñez J. M., Sáez D., 1996, *ApJ*, 469, 11
 Quilis V., Moore B., Bower R. G., 2000, *Sci*, 288, 1617
 Quilis V., Bower R. G., Balogh M. L., 2001, *MNRAS*, 328, 1091
 Rasio F. A., Shapiro S. L., 1991, *ApJ*, 377, 559
 Ritchie B. W., Thomas P. A., 2001, *MNRAS*, 323, 743
 Schüssler M., Schmitt D., 1981, *A&A*, 97, 373
 Semelin B., Combes F., 2002, *A&A*, 388, 829
 Somerville R. S., Primack J. R., 1999, *MNRAS*, 310, 1087
 Sommer-Larsen J., Dolgov A., 2001, *ApJ*, 551, 608
 Sommer-Larsen J., Götz M., Portinari L., preprint (astro-ph/0204366)
 Springel V., Hernquist L., 2002, *MNRAS*, 333, 649
 Springel V., Hernquist L., 2003, *MNRAS*, 339, 289
 Springel V., Yoshida N., White S. D. M., 2001, *New Astron.*, 6, 79
 Steinmetz M., 1996, *MNRAS*, 278, 1005
 Steinmetz M., Müller E., 1993, *A&A*, 268, 391
 Steinmetz M., Navarro J. F., 1999, *ApJ*, 513, 555
 Steinmetz M., Navarro J. F., 2002, *New Astron.*, 7, 155
 Sutherland R. S., Dopita M. A., 1993, *ApJS*, 88, 253
 Teyssier R., 2002, *A&A*, 385, 337
 Thacker R. J., Couchman H. M. P., 2000, *ApJ*, 545, 728
 Thacker R. J., Couchman H. M. P., 2001, *ApJ*, 555, L17
 Thacker R. J., Tittley E. R., Pearce F. R., Couchman H. M. P., Thomas P. A., 2000, *MNRAS*, 319, 619
 Theuns T., Leonard A., Efstathiou G., Pearce F. R., Thomas P. A., 1998, *MNRAS*, 301, 478
 Thomas P. A., Couchman H. M. P., 1992, *MNRAS*, 257, 11
 van den Bosch F. C., 2001, *MNRAS*, 327, 133
 Weil M. L., Eke V. R., Efstathiou G., 1998, *MNRAS*, 300, 773
 White S. D. M., Rees M. J., 1978, *MNRAS*, 183, 341
 Yepes G., Kates R., Khokhlov A., Klypin A., 1997, *MNRAS*, 284, 235

This paper has been typeset from a \LaTeX file prepared by the author.